Variational method enabling simplified solutions to the linearized Boltzmann equation for oscillatory gas flows

Daniel R. Ladiges and John E. Sader*

ARC Centre of Excellence in Exciton Science, School of Mathematics and Statistics, The University of Melbourne, Victoria 3010, Australia

(Received 20 September 2017; published 16 May 2018)

Nanomechanical resonators and sensors, operated in ambient conditions, often generate low-Mach-number oscillating rarefied gas flows. Cercignani [C. Cercignani, J. Stat. Phys. **1**, 297 (1969)] proposed a variational principle for the linearized Boltzmann equation, which can be used to derive approximate analytical solutions of steady (time-independent) flows. Here we extend and generalize this principle to unsteady oscillatory rarefied flows and thus accommodate resonating nanomechanical devices. This includes a mathematical approach that facilitates its general use and allows for systematic improvements in accuracy. This formulation is demonstrated for two canonical flow problems: oscillatory Couette flow and Stokes' second problem. Approximate analytical formulas giving the bulk velocity and shear stress, valid for arbitrary oscillation frequency, are obtained for Couette flow. For Stokes' second problem, a simple system of ordinary differential equations is derived which may be solved to obtain the desired flow fields. Using this framework, a simple and accurate formula is provided for the shear stress at the oscillating boundary, again for arbitrary frequency, which may prove useful in application. These solutions are easily implemented on any symbolic or numerical package, such as *Mathematica* or MATLAB, facilitating the characterization of flows produced by nanomechanical devices and providing insight into the underlying flow physics.

DOI: 10.1103/PhysRevFluids.3.053401

I. INTRODUCTION

Continued improvement in nanofabrication techniques has led to a proliferation of new devices which operate at the nanoscale. Applications include molecular-scale mass measurement [1–3], imaging with atomic resolution [4,5], microscale and nanoscale measurement of fluid properties [6–8], and ultrasensitive environmental sensing [9–11]. When operated in ambient laboratory conditions, i.e., air at 1 atm, the interaction of these devices with the surrounding gas must be considered when assessing their performance. This ensures both proper device design and interpretation of measurements. While gas flows generated by macroscopic devices can be modeled using the Navier-Stokes equations, flows at nanometer scales may violate the underlying continuum assumption. We characterize the microscopic length scale dependence of the flow using the Knudsen number

$$\mathrm{Kn} \equiv \frac{\lambda}{l},$$

where l is the device size and λ is the mean free path of the gas. A second dimensionless group naturally arises due to time dependence of the flow

$$\theta \equiv \frac{\omega}{\nu},$$

*Corresponding author: jsader@unimelb.edu.au

where ω is a characteristic angular oscillation frequency of the flow and ν is the most probable collision frequency of the gas. The Navier-Stokes equations are formally valid in the binary limit $\mathrm{Kn} \to 0$ and $\theta \to 0$. Under standard laboratory conditions, nanoscale devices will typically violate the first of these conditions, while devices operated at low pressure, or with particularly high-resonant frequencies, may violate the second. Therefore, these flows must be solved using an approach that accounts for the fundamentally rarefied (noncontinuum) nature of the gas; this is afforded by the Boltzmann equation [12].

In addition to the Kn and θ parameters described above, gas flows may also be characterized by a Mach number

$$\mathrm{Ma} \equiv \frac{U_*}{c_p}, \tag{1}$$

where U_* is a characteristic mean flow speed and c_p is the most probable molecular speed; this is proportional to the speed of sound in the gas. Flows generated by nanoscale devices typically exhibit $\mathrm{Ma} \ll 1$ and as such may be modeled using the linearized Boltzmann equation.

The linearized Boltzmann equation is analytically intractable in all but the simplest cases. Additionally, its high dimensionality and the presence of discontinuities make numerical analysis unusually difficult. For this reason, variational techniques are sometimes used to obtain relatively simple analytical approximations for quantities of interest. Examples of this approach include the shear stress in Couette flow [13], the mass flow rate in plane [13] and cylindrical [14] Poiseuille flow, the drag on a sphere [15], the heat flux between concentric spheres [16], the model dependence of velocity [17] and temperature [18] slip coefficients, and the transport [19] and sound dispersion coefficients [20] of binary gas mixtures. In each of these examples, a variational principle is derived for a formulation of the Boltzmann equation tailored specifically to the problem in question. In Ref. [21] Cercignani built on this approach by deriving a general variational principle for the steady linearized Boltzmann equation. This principle has since been applied to problems such as plane Poiseuille flow with arbitrary boundary conditions [22,23], combined Couette-Poiseuille flow [24], and with higher-order velocity slip coefficients [25,26].

In this article we extend Cercignani's variational principle [21] to flows that exhibit oscillatory (time-dependent) behavior. This is achieved by generalizing the principle from one that focuses on real-valued functions to complex-valued functions which solve the linearized Boltzmann equation in the frequency domain. Cercignani's variational principle is briefly summarized in the next section and its generalization to frequency-domain solutions is given in Sec. III.

When applying Cercignani's variational method [21] (for steady flows), a trial function is selected that approximates the true functional form of the solution in both the spatial and particle velocity domains. This function includes arbitrary constants that are determined by applying the variational principle, yielding a simple approximation of the flow. Although there is an error associated with this solution, it may be shown that some specific physical quantities display a quadratic dependence on this error. Improved accuracy for these quantities is therefore obtained, relative to the overall accuracy of the solution; this is discussed further in Sec. II A.

Using the above approach, some prior knowledge of the flow is necessary to select an appropriate trial function. Although this may be straightforward for steady flows, it is often difficult for oscillatory flows that generally exhibit a more complex spatial dependence. To overcome this limitation, we present a systematic method of solution in Sec. IV, in which the distribution function's form is specified only in particle velocity space, with no prior knowledge of the flow's spatial dependence being required. This defines a spectral method similar[1] to that described in Ref. [28], where a

[1]In the case where $\theta = 0$, numerical results suggest that the two methods are identical, although we have not proven this. For arbitrary θ, the method given in Sec. 7.3 of Ref. [27], which is similar to that given in in Ref. [28], yields numerically identical results, although once again we have not proven that the methods are equivalent.

Galerkin approach is used to solve the steady linearized Boltzmann equation. Note that where previous applications of the variational principle (mentioned above) have focused on a quantity of interest which can be found with quadratic error, here we are using the principle to derive a general method which simplifies the selection of a trial function.

This method is demonstrated in Sec. V A for the Bhatnagar-Gross-Krook (BGK) kinetic model, though it can be used for any collision operator. First, the unsteady variational principle is used to derive analytical solutions for oscillatory Couette flow. The validity of these formulas is explored by comparison to slip solutions (in the near-continuum regime) and full numerical solution to the Boltzmann equation. This is followed in Sec. V B by an illustration of the variational method's ability to transform the Boltzmann equation into a simpler system of differential equations that depends on spatial variables only, for Stokes' second problem. Such a transformation facilitates solution through use of standard solution methods for systems of first-order ordinary differential equations. Finally, an analytic solution of these equations is used to derive a simple and accurate formula for the shear stress on the oscillating surface.

II. CERCIGNANI'S VARIATIONAL METHOD

The method presented here for unsteady rarefied flows is founded on the variational principle of Cercignani [21], which is also discussed in Refs. [29,30]. We therefore begin by summarizing some key results of this previous theory.

A. General theory

To begin, the (general) equation

$$\mathcal{L}[h] = s \tag{2}$$

is specified, where $\mathcal{L}$ is some linear operator, s is a source term, and h is the unknown real-valued function to be determined. Next the existence of a linear scalar product $\langle\,,\rangle$ is assumed such that

$$\langle \mathcal{L}[p], q\rangle = \langle p, \mathcal{L}[q]\rangle, \tag{3}$$

where p and q are functions in the space operated on by $\langle\,,\rangle$; h is included in this space. Finally, we define the functional

$$J(h) = \langle h, \mathcal{L}[h]\rangle - 2\langle s, h\rangle. \tag{4}$$

Taking a solution of Eq. (2), h, and adding an error term ϑ gives

$$\hat{h} = h + \vartheta, \tag{5}$$

which upon insertion into Eq. (4) yields

$$J(\hat{h}) = \langle h + \vartheta, \mathcal{L}[h + \vartheta]\rangle - 2\langle s, h + \vartheta\rangle = J(h) + \langle \vartheta, \mathcal{L}[\vartheta]\rangle. \tag{6}$$

This gives rise to two useful properties. (i) The solution to Eq. (2), where $\vartheta = 0$, may now be characterized as an extremum of Eq. (6), i.e., a stationary point of $J(\hat{h})$. (ii) The value of $J(\hat{h})$ varies quadratically with the error in the trial function (5). When $J(\hat{h})$ can be related to a physical quantity, this may therefore be determined with error $O(\vartheta^2)$. Note that although both properties (i) and (ii) are used in Refs. [13–26], only property (i) holds for the extended variational principle discussed in Sec. III. Application of this general theory to the steady linearized Boltzmann equation is discussed next.

B. Application to the steady linearized Boltzmann equation

The Boltzmann equation describes the evolution of the number density distribution function of gas particles $f(\mathbf{c}_*, \mathbf{x}_*)$, where $\mathbf{c}_*$ is particle velocity and $\mathbf{x}_*$ is spatial position. For brevity, henceforth we abbreviate "number density distribution function" to "distribution function." An asterisk indicates

an unscaled variable throughout. For low-Mach-number flows associated with nanoscale devices, this function may be expressed as a small perturbation h from some global equilibrium state

$$f(\mathbf{c}_*,\mathbf{x}_*) = \bar{f}^{\mathrm{eq}}(\mathbf{c}_*)[1 + h(\mathbf{c}_*,\mathbf{x}_*)], \tag{7}$$

where the global equilibrium $\bar{f}^{\mathrm{eq}}$ is that of the gas at rest, given by the Maxwell-Boltzmann distribution

$$\bar{f}^{\mathrm{eq}}(\mathbf{c}_*) = \frac{n_0}{(2\pi RT_0)^{3/2}}\exp\left(-\frac{c_*^2}{2RT_0}\right), \tag{8}$$

where $c_*^2 = \mathbf{c}_* \cdot \mathbf{c}_*$, R is the specific gas constant, and n_0 and T_0 are the equilibrium number density and temperature, respectively. Bulk properties of the gas flow follow similarly, giving (for example),

$$n(\mathbf{x}_*) = n_0[1 + \sigma(\mathbf{x}_*)], \quad T(\mathbf{x}_*) = T_0[1 + \kappa(\mathbf{x}_*)], \tag{9}$$

where σ and κ are the local number density and temperature perturbations, respectively. These representations enable linearization of the Boltzmann equation for small Ma.

We scale the particle velocity by the most probable particle speed, i.e., $\mathbf{c}_* = \mathbf{c}\sqrt{2RT_0}$, and all spatial coordinates by a geometric length scale, i.e., $\mathbf{x}_* = \mathbf{x}l$; variables without an asterisk denote the scaled coordinates. The steady linearized Boltzmann equation is then given by

$$\mathrm{Kn}\mathbf{c} \cdot \frac{\partial h}{\partial \mathbf{x}} = L[h] + s, \quad \mathbf{x} \in \Omega, \quad \mathbf{c} \in \mathbb{R}^3, \tag{10}$$

where L is a linearized collision operator, s is a source term, and Ω represents the spatial domain (which may vary from one to three dimensions). The (scaled) linearized BGK [12,31] operator is

$$L[h(\mathbf{c},\mathbf{x})] = h^{\mathrm{eq}}(\mathbf{c},\mathbf{x}) - h(\mathbf{c},\mathbf{x}), \tag{11}$$

where h^{eq} is the local equilibrium perturbation

$$h^{\mathrm{eq}}(\mathbf{c},\mathbf{x}) = \sigma + 2\mathbf{c} \cdot \mathbf{u} + \left(c^2 - \tfrac{3}{2}\right)\kappa, \tag{12}$$

and

$$\begin{aligned}
\sigma(\mathbf{x}) &= \frac{1}{\pi^{3/2}}\int_{\mathbb{R}^3} h(\mathbf{c}_1,\mathbf{x})e^{-c_1^2}d\mathbf{c}_1, \quad \mathbf{u}(\mathbf{x}) = \frac{1}{\pi^{3/2}}\int_{\mathbb{R}^3} \mathbf{c}_1 h(\mathbf{c}_1,\mathbf{x})e^{-c_1^2}d\mathbf{c}_1, \\
\kappa(\mathbf{x}) &= \frac{2}{3\pi^{3/2}}\int_{\mathbb{R}^3}\left(c_1^2 - \frac{3}{2}\right)h(\mathbf{c}_1,\mathbf{x})e^{-c_1^2}d\mathbf{c}_1
\end{aligned} \tag{13}$$

give the scaled local density, velocity, and temperature perturbations, respectively. The BGK operator is used here for simplicity; however, the methods outlined in this article may be applied to any linearized collision operator.

The boundary conditions associated with Eq. (10) are given by the general form

$$h^+(\mathbf{c},\mathbf{x}) = B[h^-(\mathbf{c},\mathbf{x})] + s_b(\mathbf{c},\mathbf{x}), \quad \mathbf{x} \in \partial\Omega, \tag{14}$$

where h^+ and h^- are the distribution function perturbations for outbound ($\mathbf{c} \cdot \mathbf{n} > 0$) and inbound ($\mathbf{c} \cdot \mathbf{n} < 0$) particle velocities to the boundary, respectively; $\mathbf{n}$ is the unit normal vector to the boundary pointing into the gas. The operator B transforms functions defined for $\mathbf{c} \cdot \mathbf{n} < 0$ to functions defined over $\mathbf{c} \cdot \mathbf{n} > 0$. The term s_b is a boundary source term with no dependence on the inbound function. We note that this general boundary condition introduces a discontinuity in particle velocity space between h^+ and h^-.

We employ the diffuse boundary condition for a solid boundary, which in its linearized form is

$$h^+(\mathbf{c},\mathbf{x}) = \left\{\sigma_b + 2\mathbf{c} \cdot \mathbf{u}_b + \left(c^2 - \tfrac{3}{2}\right)\kappa_b\right\}, \quad \mathbf{x} \in \partial\Omega, \tag{15}$$

where $\mathbf{u}_b$ and κ_b are the velocity and the temperature perturbations of the boundary. The boundary density perturbation σ_b is obtained by enforcing mass conservation at the wall [12],

$$\sigma_b = \mathbf{u}_b \cdot \mathbf{n}\sqrt{\pi} - \frac{1}{2}\kappa_b - \frac{2}{\pi}\int_{\mathbf{c}_1\cdot\mathbf{n}<0} h^-(\mathbf{c}_1)e^{-c_1^2}\mathbf{c}_1 \cdot \mathbf{n}\, d\mathbf{c}_1. \tag{16}$$

While the diffuse boundary condition is chosen for simplicity, more general boundary conditions such as those of Maxwell [32] or Cercignani and Lampis [33] can also be used. Open boundaries, where no solid wall is present, are modeled as an interface with a gas at equilibrium. In such cases, σ_b, $\mathbf{u}_b$, and κ_b are the local density perturbation, velocity, and temperature perturbation of this (external) gas, respectively.

Equation (10) is then expressed in the operator form

$$D[h] - L[h] = s, \tag{17}$$

where D represents the advection term on the left-hand side of Eq. (10). The operation used in Eq. (3) is defined as the scalar product

$$\langle p,q\rangle = \int_\Omega \int_{\mathbb{R}^3} p(\mathbf{c},\mathbf{x})q(-\mathbf{c},\mathbf{x})e^{-c^2}\, d\mathbf{c}\, d\mathbf{x}, \tag{18}$$

where p and q are taken to be real-valued functions. Both the collision operator L and advection operator D possess the symmetry of Eq. (3) when the operation defined in Eq. (18) is used, i.e.,

$$\langle L[p],q\rangle = \langle p,L[q]\rangle, \quad \langle D[p],q\rangle = \langle p,D[q]\rangle. \tag{19}$$

The reader is directed to Refs. [21,29,30] for proof and further discussion of Eq. (19).

Given a trial solution $\hat{h}$ that satisfies the boundary condition (14), the solution to Eq. (10) is then specified by the stationary point of

$$J(\hat{h}) = \langle \hat{h}, D[\hat{h}] - L[\hat{h}]\rangle - 2\langle \hat{h}, s\rangle. \tag{20}$$

Equation (20) is the required result that enables calculation of approximate solutions to the linearized Boltzmann equation for steady flows.

III. GENERALIZATION OF THE VARIATIONAL METHOD TO THE FREQUENCY-DOMAIN BOLTZMANN EQUATION

The unsteady linearized Boltzmann equation is

$$\frac{\partial h}{\partial t} + \mathrm{Kn}\mathbf{c}\cdot\frac{\partial h}{\partial \mathbf{x}} = L[h] + s, \quad \mathbf{x}\in\Omega,\ \mathbf{c}\in\mathbb{R}^3, \tag{21}$$

where the time variable is scaled by the most probable particle collision time, i.e., $t = t_*\nu$. Due to linearity, the distribution function perturbation h takes the time dependence

$$h(\mathbf{c}_*,\mathbf{x}_*,t_*|\omega) = \tilde{h}(\mathbf{c}_*,\mathbf{x}_*|\omega)e^{-i\omega t_*}, \tag{22}$$

where ω is the angular frequency of the flow, i is the imaginary unit, and $\tilde{h}$ is the spatial and particle velocity dependence of the (complex-valued) distribution function; the tilde will be used henceforth to denote this component. Inserting Eq. (22) into Eq. (21) yields the frequency-domain Boltzmann equation

$$-i\theta\tilde{h} + \mathrm{Kn}\mathbf{c}\cdot\frac{\partial \tilde{h}}{\partial \mathbf{x}} = L[\tilde{h}] + \tilde{s}. \tag{23}$$

The frequency-domain BGK operator follows directly from Eq. (13),

$$L[\tilde{h}] = \tilde{h}^{\mathrm{eq}}(\mathbf{c},\mathbf{x}) - \tilde{h}(\mathbf{c},\mathbf{x}), \tag{24}$$

where

$$\tilde{h}^{\mathrm{eq}}(\mathbf{c},\mathbf{x}) = \tilde{\sigma} + 2\mathbf{c}\cdot\tilde{\mathbf{u}} + \left(c^2 - \tfrac{3}{2}\right)\tilde{\kappa}, \tag{25}$$

with

$$\tilde{\sigma}(\mathbf{x}) = \frac{1}{\pi^{3/2}}\int_{\mathbb{R}^3}\tilde{h}(\mathbf{c}_1)e^{-c_1^2}d\mathbf{c}_1, \quad \tilde{\mathbf{u}}(\mathbf{x}) = \frac{1}{\pi^{3/2}}\int_{\mathbb{R}^3}\mathbf{c}_1\tilde{h}(\mathbf{c}_1)e^{-c_1^2}d\mathbf{c}_1,$$
$$\tilde{\kappa}(\mathbf{x}) = \frac{2}{3\pi^{3/2}}\int_{\mathbb{R}^3}\left(c_1^2 - \frac{3}{2}\right)\tilde{h}(\mathbf{c}_1)e^{-c_1^2}d\mathbf{c}_1. \tag{26}$$

Note that the frequency-domain Boltzmann equation (23) is the equation governing a single Fourier component of a flow of arbitrary time dependence. If a flow is driven with sinusoidal time dependence θ, the equation yields the solution at large t, i.e., after any startup effects have dissipated. Flows of arbitrary time dependence can in principle be reconstructed from solutions for multiple θ values; an example of this approach is given in Ref. [34].

In the operator notation of Eq. (17), Eq. (23) becomes

$$-i\theta\tilde{h} + D[\tilde{h}] - L[\tilde{h}] = \tilde{s}. \tag{27}$$

The form of the boundary condition in Eq. (14) is unchanged, with h simply replaced by $\tilde{h}$.

Next we separate the real and imaginary parts of Eq. (27),

$$D[\tilde{h}_{\mathrm{Re}}] - L[\tilde{h}_{\mathrm{Re}}] = -\theta\tilde{h}_{\mathrm{Im}} + \tilde{s}_{\mathrm{Re}}, \tag{28a}$$
$$D[\tilde{h}_{\mathrm{Im}}] - L[\tilde{h}_{\mathrm{Im}}] = \theta\tilde{h}_{\mathrm{Re}} + \tilde{s}_{\mathrm{Im}}. \tag{28b}$$

The functional specified by Eq. (20) is then obtained separately for the real and imaginary equations, giving

$$\tilde{J}_{\mathrm{Re}}(\hat{h}) = \langle\hat{h}_{\mathrm{Re}}, D[\hat{h}_{\mathrm{Re}}] - L[\hat{h}_{\mathrm{Re}}]\rangle + 2\langle\hat{h}_{\mathrm{Re}}, \theta\hat{h}_{\mathrm{Im}} + \tilde{s}_{\mathrm{Re}}\rangle, \tag{29a}$$
$$\tilde{J}_{\mathrm{Im}}(\hat{h}) = \langle\hat{h}_{\mathrm{Im}}, D[\hat{h}_{\mathrm{Im}}] - L[\hat{h}_{\mathrm{Im}}]\rangle - 2\langle\hat{h}_{\mathrm{Im}}, \theta\hat{h}_{\mathrm{Re}} - \tilde{s}_{\mathrm{Im}}\rangle, \tag{29b}$$

where $\hat{h}$ is a complex-valued trial function that exactly satisfies the boundary conditions. Note that in the functional for the real part of the trial function (29a), the imaginary part of the trial function appears as a source term. Similarly, in Eq. (29b), the real part of the trial function appears as a source term. Following the approach of Sec. II A, Eqs. (29) may be expressed

$$\tilde{J}_{\mathrm{Re}}(\hat{h}) = \tilde{J}_{\mathrm{Re}}(\tilde{h}) + 2\theta\langle\tilde{\vartheta}_{\mathrm{Im}}, \tilde{h}_{\mathrm{Re}}\rangle + 2\theta\langle\tilde{\vartheta}_{\mathrm{Re}}, \tilde{\vartheta}_{\mathrm{Im}}\rangle + \langle\tilde{\vartheta}_{\mathrm{Re}}, \mathcal{L}[\tilde{\vartheta}_{\mathrm{Re}}]\rangle, \tag{30a}$$
$$\tilde{J}_{\mathrm{Im}}(\hat{h}) = \tilde{J}_{\mathrm{Im}}(\tilde{h}) - 2\theta\langle\tilde{\vartheta}_{\mathrm{Re}}, \tilde{h}_{\mathrm{Im}}\rangle - 2\theta\langle\tilde{\vartheta}_{\mathrm{Im}}, \tilde{\vartheta}_{\mathrm{Re}}\rangle + \langle\tilde{\vartheta}_{\mathrm{Im}}, \mathcal{L}[\tilde{\vartheta}_{\mathrm{Im}}]\rangle, \tag{30b}$$

where $\tilde{\vartheta}_{\mathrm{Re}}$ and $\tilde{\vartheta}_{\mathrm{Im}}$ are the errors in the real and imaginary components of the solution, respectively. As in Sec. II A, the stationary point in Eqs. (30) occurs when the error terms equal zero. Interestingly, the error in each functional is no longer quadratic; $\tilde{J}_{\mathrm{Re}}(\hat{h})$ varies linearly with $\tilde{\vartheta}_{\mathrm{Im}}$ and $\tilde{J}_{\mathrm{Im}}(\hat{h})$ varies linearly with $\tilde{\vartheta}_{\mathrm{Re}}$. Next we present a methodology for locating the stationary point in Eqs. (29), systematically implementing this variational principle for general oscillatory flows.

IV. METHODS OF SOLUTION

In Sec. IV A we first outline a systematic solution method that requires the functional form of the trial function $\hat{h}$ to be specified only in particle velocity space and which requires no prior knowledge of the flow field. This is followed in Sec. IV B by an approach that facilitates solutions for highly nonequilibrium flows. These techniques are used in Sec. V to derive simple approximate solutions for two canonical problems.

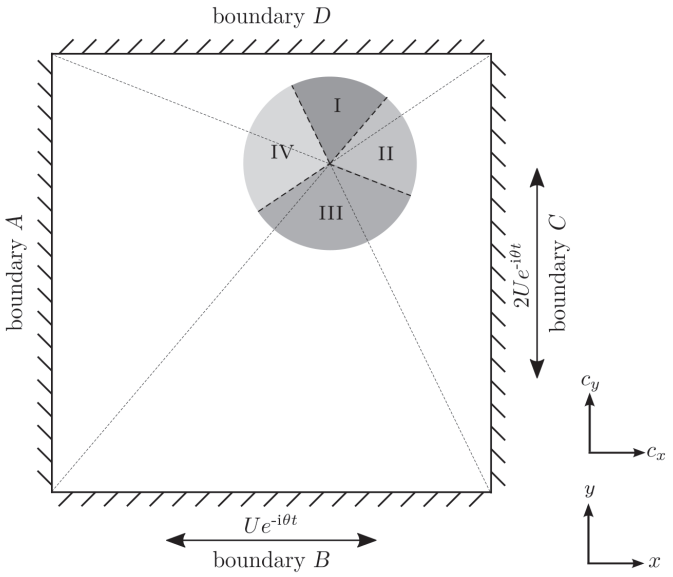

FIG. 1. Illustration of an example trial function where discontinuities in particle velocity space vary as a function of the spatial coordinates. For arbitrary position $\mathbf{x}$, particle velocities emanating from boundary A pass through shaded region II, particle velocities emanating from boundary B pass through region I, particle velocities emanating from boundary C pass through region IV, and particle velocities emanating from boundary D pass through region III. The heavy dashed lines represent discontinuities in particle velocity space. The light dashed lines trace the particle velocities from each corner of the domain to the arbitrary spatial position $\mathbf{x}$.

A. Direct solution using basis functions

1. Defining the trial function

To define the trial function $\hat{h}$, we note that the boundary condition in Eq. (14) introduces a discontinuity into the distribution function $\tilde{h}$. For each boundary in the spatial domain, with outward normal vector $\mathbf{n}$, this discontinuity occurs in particle velocity space where $\mathbf{c} \cdot \mathbf{n} = 0$. This happens because the boundary condition is only applied to particle velocities where $\mathbf{c} \cdot \mathbf{n} > 0$, i.e., to particles leaving the surface. In the free molecular limit, each discontinuity propagates into the spatial domain along characteristics emanating from the edges of its originating boundary. These characteristics are defined by the direction of particle motion, i.e.,

$$\boldsymbol{x}(\xi) = \xi \frac{\mathbf{c}}{|\mathbf{c}|} + \mathbf{x}_0, \quad \mathbf{x}_0 \in \partial\Omega, \tag{31}$$

where each characteristic is parametrized by ξ. Consequently, we separate the trial function $\hat{h}$ into segments of particle velocity space representing characteristics emerging from a given boundary. For a flow with P boundaries, there are P segments, each represented by the function $\hat{h}^{\mathrm{p}}(\mathbf{c},\mathbf{x})$. A simple example of this approach that involves straight boundary segments is illustrated in Fig. 1; boundaries of arbitrary shape are equally applicable and are discussed in the Appendix. Importantly, the functions $\hat{h}^{\mathrm{p}}(\mathbf{c},\mathbf{x})$ are zero outside of the region of particle velocity space that they represent. This produces discontinuities in the trial function $\hat{h}$ following characteristics from the edges of each boundary, as required for free molecular flow. Each segment of the trial function, i.e., $\hat{h}^{\mathrm{p}}(\mathbf{c},\mathbf{x})$, is then expanded as a linear combination of N specified (real-valued) basis functions in particle velocity

space $a_n(\mathbf{c})$ such that

$$\hat{h}^{\mathrm{p}}(\mathbf{c},\mathbf{x}) = \sum_{n=1}^{N} a_n(\mathbf{c}) m_n^{\mathrm{p}}(\mathbf{x}). \tag{32}$$

The value of the spatial functions $m_n^{\mathrm{p}}(\mathbf{x})$, for the relevant region of particle velocity space, is determined by the variational procedure detailed below.

For nonfree molecular flows, the discontinuities originating at the boundaries are removed by particle collisions as they propagate into the spatial domain; however, sharp jumps in particle velocity space remain. For highly rarefied flows, where few particle collisions occur, these jumps persist away from the boundaries, whereas for near continuum flows, there are many particle collisions and these jumps are restricted close to the boundaries. Setting the trial function to be discontinuous at the location of these jumps allows the functions $\hat{h}^{\mathrm{p}}(\mathbf{c},\mathbf{x})$ [Eq. (32)] to be specified with relatively low order. This method offers superior accuracy compared to using a single expansion to represent the whole of particle velocity space, an approach which would generally require a trial function of much higher order to capture the jumps.

By way of illustration, consider the example given in Fig. 1, a two-dimensional region bounded by $x = 0$ (boundary A), $y = 0$ (boundary B), $x = 1$ (boundary C), and $y = 1$ (boundary D). We apply the diffuse boundary condition given in Eq. (15), with boundaries A and D being stationary, boundary B oscillating in the x direction with scaled amplitude U, and boundary C oscillating in the z direction with scaled amplitude $2U$. To simplify this example, mass conservation is neglected by artificially setting $\sigma_b = 0$;[2] this condition also naturally occurs for the cases studied in later sections, but does not hold generally. This gives

$$\tilde{h}_A^+(x=0) = 0, \quad \tilde{h}_B^+(y=0) = 2Uc_x, \quad \tilde{h}_C^+(x=1) = 4Uc_z, \quad \tilde{h}_D^+(y=1) = 0 \tag{33}$$

for boundaries A, B, C, and D, respectively. The trial function is broken into $P = 4$ regions representing the characteristics emanating from each of the four boundaries,

$$\hat{h}(c_x,c_y,x,y) = \begin{cases} \hat{h}^{\mathrm{I}}(c_x,c_y,x,y), & (c_x,c_y) \in \mathrm{I} \\ \hat{h}^{\mathrm{II}}(c_x,c_y,x,y), & (c_x,c_y) \in \mathrm{II} \\ \hat{h}^{\mathrm{III}}(c_x,c_y,x,y), & (c_x,c_y) \in \mathrm{III} \\ \hat{h}^{\mathrm{IV}}(c_x,c_y,x,y), & (c_x,c_y) \in \mathrm{IV}. \end{cases} \tag{34}$$

Here segment I corresponds to particle velocities emanating from boundary B, segment II to velocities emanating from boundary A, segment III to velocities from boundary D, and segment IV to velocities from boundary C. This division is illustrated by the shaded regions in Fig. 1, for an arbitrary point in the spatial domain. We note that the location of these divisions in particle velocity space varies as a function of the spatial coordinates.

Considering the basis functions $a_n(\mathbf{c})$ to be polynomials, each segment of the trial function, as per Eq. (32), is given by

$$\hat{h}^{\mathrm{p}}(c_x,c_z,x,y) = c_x m_1^{\mathrm{p}}(x,y) + c_z m_2^{\mathrm{p}}(x,y) + c_x c_z m_3^{\mathrm{p}}(x,y), \tag{35}$$

[2]This unphysical boundary condition simplifies analysis by ignoring the perturbed particles incoming to the wall, i.e., mass conservation is not enforced.

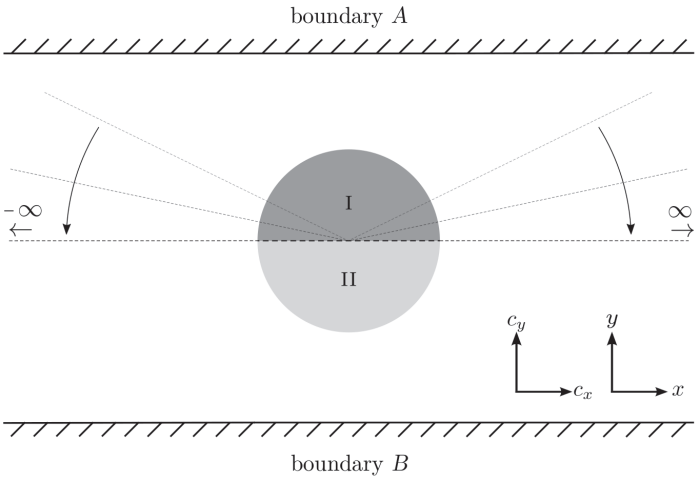

FIG. 2. Illustration of the example trial function for a simple one-dimensional flow. Here particles emanating from boundary B pass through region I, whereas region II is for particles emanating from boundary A. Unlike Fig. 1, the division of particle velocity space occurs at $c_y = 0$ regardless of the spatial location. This is because characteristics emanating from each plate become parallel to the plate as $x \to \pm\infty$, regardless of the value of y.

where we have used $N = 3$ basis functions. Combining Eqs. (34) and (35) yields a discontinuous (piecewise) trial function defined in four segments of particle velocity space,

$$\hat{h}(c_x,c_z,x,y) = \begin{cases} c_x m_1^{\mathrm{I}}(x,y) + c_y m_2^{\mathrm{I}}(x,y) + c_x c_y m_3^{\mathrm{I}}(x,y), & (c_x,c_y) \in \mathrm{I} \\ c_x m_1^{\mathrm{II}}(x,y) + c_y m_2^{\mathrm{II}}(x,y) + c_x c_y m_3^{\mathrm{II}}(x,y), & (c_x,c_y) \in \mathrm{II} \\ c_x m_1^{\mathrm{III}}(x,y) + c_y m_2^{\mathrm{III}}(x,y) + c_x c_y m_3^{\mathrm{III}}(x,y), & (c_x,c_y) \in \mathrm{III} \\ c_x m_1^{\mathrm{IV}}(x,y) + c_y m_2^{\mathrm{IV}}(x,y) + c_x c_y m_3^{\mathrm{IV}}(x,y), & (c_x,c_y) \in \mathrm{IV}. \end{cases} \tag{36}$$

At each boundary, the conditions in Eq. (33) are applied by specifying the value of the m_n^{p} functions which belong to the regions of particle velocity space where $\mathbf{c} \cdot \mathbf{n} > 0$, i.e., the functions defined for particle velocities emanating from that boundary. For boundary A this gives

$$m_1^{\mathrm{II}}(0,y) = 0, \quad m_2^{\mathrm{II}}(0,y) = 0, \quad m_3^{\mathrm{II}}(0,y) = 0,$$

whereas boundary B yields

$$m_1^{\mathrm{I}}(x,0) = 2U, \quad m_2^{\mathrm{I}}(x,0) = 0, \quad m_3^{\mathrm{I}}(x,0) = 0,$$

while boundary C gives

$$m_1^{\mathrm{IV}}(1,y) = 0, \quad m_2^{\mathrm{IV}}(1,y) = 4U, \quad m_3^{\mathrm{IV}}(1,y) = 0,$$

and for boundary D we have

$$m_1^{\mathrm{III}}(x,1) = 0, \quad m_2^{\mathrm{III}}(x,1) = 0, \quad m_3^{\mathrm{III}}(x,1) = 0.$$

A second example is given in Fig. 2, where the domain for a one-dimensional flow is shown. Here characteristics emanating from boundary A towards boundary B are contained in particle velocity space segment II, i.e., $c_y < 0$. Segment I represents characteristics originating at boundary B, i.e., $c_y > 0$. Unlike the higher-dimensional example in Fig. 1, the resulting discontinuity in particle velocity space (at $c_y = 0$) is obviously independent of the spatial location. This greatly simplifies analysis in the following sections, compared to the more general case in Fig. 1. As mentioned previously, the focus of this article is to obtain simple solutions for one-dimensional flows. Because

these flows feature domains similar to that shown in Fig. 2, we proceed by assuming a trial function where the divisions in particle velocity space are independent of the spatial coordinates.

2. *Applying the variational principle*

Inserting the trial function into Eq. (29) and integrating over particle velocity space gives

$$\tilde{J}_{\mathrm{Re}}(\hat{h}) = \int_{\Omega} M_{\mathrm{Re}}\big(m^{\mathrm{p}}_{\mathrm{Re},n}(\mathbf{x}), m^{\mathrm{p}}_{\mathrm{Im},n}(\mathbf{x})\big)d\mathbf{x}, \tag{37a}$$

$$\tilde{J}_{\mathrm{Im}}(\hat{h}) = \int_{\Omega} M_{\mathrm{Im}}\big(m^{\mathrm{p}}_{\mathrm{Re},n}(\mathbf{x}), m^{\mathrm{p}}_{\mathrm{Im},n}(\mathbf{x})\big)d\mathbf{x}, \tag{37b}$$

where the resulting integrands M_{Re} and M_{Im} now depend exclusively on the spatial variables; explicit expressions for M are not provided here, but examples are given in the next section. The stationary point of $\tilde{J}$ is given by the simultaneous Euler-Lagrange equations

$$\frac{\partial M_{\mathrm{Re}}}{\partial m^{\mathrm{p}}_{\mathrm{Re},n}} - \frac{\partial}{\partial \mathbf{x}}\frac{\partial M_{\mathrm{Re}}}{\partial m^{\mathrm{p}}_{\mathbf{x},\mathrm{Re},n}} = 0, \quad \frac{\partial M_{\mathrm{Im}}}{\partial m^{\mathrm{p}}_{\mathrm{Im},n}} - \frac{\partial}{\partial \mathbf{x}}\frac{\partial M_{\mathrm{Im}}}{\partial m^{\mathrm{p}}_{\mathbf{x},\mathrm{Im},n}} = 0 \tag{38}$$

for $1 \leqslant n \leqslant N$ and $1 \leqslant \mathrm{p} \leqslant P$, giving $2NP$ real-valued equations. Here

$$\frac{\partial}{\partial \mathbf{x}}\frac{\partial M}{\partial m^{\mathrm{p}}_{\mathbf{x},n}} = \frac{\partial}{\partial x}\frac{\partial M}{\partial m^{\mathrm{p}}_{x,n}} + \frac{\partial}{\partial y}\frac{\partial M}{\partial m^{\mathrm{p}}_{y,n}} + \frac{\partial}{\partial z}\frac{\partial M}{\partial m^{\mathrm{p}}_{z,n}}$$

and $m^{\mathrm{p}}_{x,n}$, $m^{\mathrm{p}}_{y,n}$, and $m^{\mathrm{p}}_{z,n}$ indicate the derivatives of the functions m^{p}_{n} with respect to each of the spatial coordinates. Recall that in the real functional (29a) the imaginary part of the trial function is treated as a source term. Similarly, in the imaginary functional (29b) the real part of the trial function is considered a source term. The functional derivative of M_{Re} is therefore taken only with respect to the functions $m^{\mathrm{p}}_{\mathrm{Re},n}$ and $m^{\mathrm{p}}_{\mathbf{x},\mathrm{Re},n}$ and the derivative of M_{Im} is taken using only the functions $m^{\mathrm{p}}_{\mathrm{Im},n}$ and $m^{\mathrm{p}}_{\mathbf{x},\mathrm{Im},n}$.

An alternative derivation of Eq. (38) is given by inserting the complex-valued trial function $\hat{h}$ directly into the functional originally defined for the steady case [Eq. (4)]. In this case the linear operator is given by

$$\mathcal{L}[\hat{h}] = D[\hat{h}] - L[\hat{h}] - i\theta\hat{h}, \tag{39}$$

yielding

$$\tilde{J}(\hat{h}) = \langle \hat{h}, D[\hat{h}] - L[\hat{h}] - i\theta\hat{h}\rangle + 2\langle \hat{h}, s\rangle. \tag{40}$$

This gives NP complex-valued Euler-Lagrange equations

$$\frac{\partial M}{\partial m^{\mathrm{p}}_{n}} - \frac{\partial}{\partial \mathbf{x}}\frac{\partial M}{\partial m^{\mathrm{p}}_{\mathbf{x},n}} = 0, \quad 1 \leqslant n \leqslant N,\ 1 \leqslant \mathrm{p} \leqslant P, \tag{41}$$

where M is now the integrand of the functional in Eq. (40), i.e.,

$$\tilde{J}(\hat{h}) = \int_{\Omega} M\big(m^{\mathrm{p}}_{n}(\mathbf{x})\big)d\mathbf{x}.$$

Taking the real and imaginary parts of Eq. (41) gives Eq. (38). Although this derivation is simpler, the existence of the required stationary point is more clearly illustrated using the approach given by Eqs. (29) and (37).

Solving Eq. (38) or (41) gives a solution to the frequency-domain Boltzmann equation; steady flows are easily modeled using this approach with $\theta = 0$. Increasing N systematically refines these solutions. For small values of N, simple equations are obtained which can yield good approximations to full numerical solutions of the Boltzmann equation (see Sec. V).

B. Decomposition using the gain-free solution

Oscillatory flows near solid walls are characterized by regions of strong departure from equilibrium, which spread further into the spatial domain as the flow becomes more rarefied. To accommodate this effect, we present a solution method for the variational principle that naturally handles the intrinsic collisionless flows immediately near solid boundaries.

In the collisionless binary limit $\mathrm{Kn} \to \infty$ and $\theta \to \infty$, the Boltzmann equation becomes

$$\mathrm{Kn}\mathbf{c} \cdot \frac{\partial \tilde{h}}{\partial \mathbf{x}} = i\theta \tilde{h}. \tag{42}$$

The form of Eq. (42) is essentially unchanged by the inclusion of the loss term $-h$ from the BGK operator [35,36],

$$\mathrm{Kn}\mathbf{c} \cdot \frac{\partial \tilde{h}}{\partial \mathbf{x}} = (i\theta - 1)\tilde{h}. \tag{43}$$

This equation differs from the frequency-domain Boltzmann equation only by the absence of the gain term $\tilde{h}^{\mathrm{eq}}$ in the collision operator [see Eqs. (23) and (24)]. We therefore designate Eq. (43) the gain-free Boltzmann equation. This equation may be solved along characteristics specified by Eq. (31), giving

$$\tilde{h}_{\mathrm{gf}} = \tilde{h}^{+}(\mathbf{x}_0) \exp\left(\frac{i\theta - 1}{\mathrm{Kn}|\mathbf{c}|}\xi\right), \tag{44}$$

with the subscript gf indicating gain-free. Equation (44) becomes increasingly oscillatory as $|\mathbf{c}| \to 0$. This can be difficult to handle numerically, and its explicit inclusion here improves approximation using the variational method.

To incorporate this gain-free solution into the overall solution of the Boltzmann equation, we insert a solution of the form [35,36]

$$\tilde{h} = \tilde{h}_1 + \tilde{h}_{\mathrm{gf}} \tag{45}$$

into the frequency-domain Boltzmann equation (23), giving

$$\mathrm{Kn}\mathbf{c} \cdot \frac{\partial \tilde{h}_1}{\partial \mathbf{x}} = (i\theta - 1)\tilde{h}_1 + \tilde{h}_1^{\mathrm{eq}} + \tilde{h}_{\mathrm{gf}}^{\mathrm{eq}}, \tag{46}$$

where $\tilde{h}_{\mathrm{gf}}^{\mathrm{eq}}$ arises from the gain term in the collision operator and is derived by inserting $\tilde{h} = \tilde{h}_{\mathrm{gf}}$ into Eq. (26) and subsequently Eq. (25). Equation (46) may be solved for $\tilde{h}_1$ using the variational approach described in Sec. IV A, with $\tilde{h}_{\mathrm{gf}}^{\mathrm{eq}}$ treated as a source term, i.e., $\tilde{s} = \tilde{h}_{\mathrm{gf}}^{\mathrm{eq}}$. The performance of this approach relative to that of the direct method in Sec. IV A (which does not make use of the gain-free solution) is explored in the next section.

V. RESULTS AND DISCUSSION

We now apply the methods described in Sec. IV to two one-dimensional flows: oscillatory Couette flow and Stokes' second problem. First, oscillatory Couette flow is used to illustrate the relative accuracies of the two methods (presented in Secs. IV A and IV B), for which approximate formulas valid for arbitrary Kn and θ are derived. We also compare solutions obtained using the approach in Sec. IV A to those obtained using the Navier-Stokes equation in conjunction with a slip boundary condition. Second, the approaches of Secs. IV B and IV A are used to derive a simple system of equations approximating Stokes' second problem. The first of these is easily solved using standard numerical techniques, while the second yields an analytic solution that may prove valuable in application.

A. Oscillatory Couette flow

The flow geometry is bounded by two infinite parallel walls at $y = 0$ and $y = 1$ (see Fig. 3). The upper wall oscillates in the x direction with scaled velocity amplitude U, where $U_* = U\sqrt{2RT_0}$,

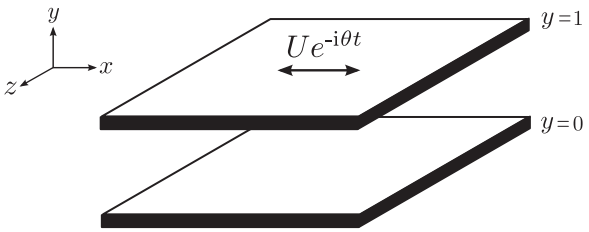

FIG. 3. Schematic of the oscillatory Couette flow geometry showing the coordinate system and geometry.

and scaled angular frequency θ, while the lower wall is stationary. The domain is unbounded in the x and z directions. The solid walls are assumed to be diffusely reflecting, the boundary conditions of which then follow from Eq. (15), with

$$\hat{h}^{+}(c_x,c_y,y) = \begin{cases} 2Uc_x, & y=1, \quad c_y<0 \\ 0, & y=0, \quad c_y>0. \end{cases} \tag{47}$$

The solution methods in Sec. IV are now used to solve this flow problem.

1. Direct solution using polynomial basis functions

We first consider the direct approach of Sec. IV A that uses polynomials for the basis functions $a_n(\mathbf{c})$ in Eq. (32). As per the example in Fig. 2, the trial function is first separated into two distinct parts corresponding to particle velocities in the upward ($c_y > 0$) and downward ($c_y < 0$) directions,

$$\hat{h}(c_x,c_y,y) = \begin{cases} \hat{h}^{\mathrm{I}}(c_x,c_y,y), & c_y>0 \\ \hat{h}^{\mathrm{II}}(c_x,c_y,y), & c_y<0, \end{cases} \tag{48}$$

where the velocity space dependence of the resulting two functions is expanded using polynomials in c_y to give

$$\hat{h}^{\mathrm{I}}(c_x,c_y,y) = c_x \sum_{n=1}^{N} m_n^{\mathrm{I}}(y) c_y^{n-1}, \tag{49a}$$

$$\hat{h}^{\mathrm{II}}(c_x,c_y,y) = c_x \sum_{n=1}^{N} m_n^{\mathrm{II}}(y) c_y^{n-1}. \tag{49b}$$

For consistency, each component in Eq. (49) uses the same polynomial degree N. The linear dependence in Eq. (49) on c_x follows directly from the linearized Boltzmann equation (23) for this flow. The components of $\hat{h}$ emanating from $y=0$ and $y=1$ contain the (as yet unspecified) functions $m_n^{\mathrm{I}}(y)$ and $m_n^{\mathrm{II}}(y)$.

To solve for $\hat{h}$, we locate the stationary point of the functional specified in Eq. (37), with respect to the $2N$ functions m_n^{I} and m_n^{II}. Using the definition of Eq. (48), the functional is

$$\tilde{J} = \int_{\Omega} M(\hat{h}^{\mathrm{I}},\hat{h}^{\mathrm{II}}) d\mathbf{x}, \tag{50}$$

where the integrand M is

$$\begin{aligned} M(\hat{h}^{\mathrm{I}},\hat{h}^{\mathrm{II}}) = &\int_{c_y<0} \hat{h}^{\mathrm{II}}(\mathbf{c}) \left\{ -\mathrm{Kn} c_y \frac{\partial}{\partial y} \hat{h}^{\mathrm{I}}(-\mathbf{c}) - L^{\mathrm{I}}[\hat{h}(-\mathbf{c})] - i\theta \hat{h}^{\mathrm{I}}(-\mathbf{c}) \right\} e^{-c^2} d\mathbf{c} \\ &+ \int_{c_y>0} \hat{h}^{\mathrm{I}}(\mathbf{c}) \left\{ -\mathrm{Kn} c_y \frac{\partial}{\partial y} \hat{h}^{\mathrm{II}}(-\mathbf{c}) - L^{\mathrm{II}}[\hat{h}(-\mathbf{c})] - i\theta \hat{h}^{\mathrm{II}}(-\mathbf{c}) \right\} e^{-c^2} d\mathbf{c}. \end{aligned} \tag{51}$$

Note that the integrals in Eq. (51) are performed over the entire $\mathbb{R}^3$ particle velocity space where the indicated condition on c_y applies. Because polynomial basis functions and the BGK collision operator are used, these integrals are performed analytically; use of more complicated collision operators, such as that for hard spheres, would normally require numerical computation. Recall that the operation used to generate Eq. (51) entails reversal of the velocity coordinate [see Eq. (18)], giving

$$\hat{h}(-\mathbf{c}) = \begin{cases} \hat{h}^{\mathrm{II}}(-\mathbf{c}), & c_y > 0 \\ \hat{h}^{\mathrm{I}}(-\mathbf{c}), & c_y < 0. \end{cases} \tag{52}$$

The BGK collision terms then become

$$L^{\mathrm{I}}[\hat{h}(-\mathbf{c})] = -2c_x\tilde{u}_x - \hat{h}^{\mathrm{I}}(-\mathbf{c}), \quad L^{\mathrm{II}}[\hat{h}(-\mathbf{c})] = -2c_x\tilde{u}_x - \hat{h}^{\mathrm{II}}(-\mathbf{c}), \tag{53}$$

where

$$\tilde{u}_x = \frac{1}{\pi^{3/2}}\int_{c_{y,1}>0} c_{y,1}\hat{h}^{\mathrm{I}}(\mathbf{c}_1)e^{-c_1^2}d\mathbf{c}_1 + \frac{1}{\pi^{3/2}}\int_{c_{y,1}<0} c_{y,1}\hat{h}^{\mathrm{II}}(\mathbf{c}_1)e^{-c_1^2}d\mathbf{c}_1. \tag{54}$$

Finally, M [Eq. (51)] is inserted into Eq. (41) to obtain the required system of ordinary differential equations (Euler-Lagrange equations) for the m_n^{I} and m_n^{II} functions comprising $\hat{h}$. In terms of the trial function (48), the diffuse boundary conditions for Couette flow (47) are given by

$$\hat{h}^{\mathrm{II}}(y=1) = 2Uc_x, \quad \hat{h}^{\mathrm{I}}(y=0) = 0. \tag{55}$$

This implies $m_1^{\mathrm{II}}(1) = 2U$ and $m_n^{\mathrm{II}}(1) = 0$ for $n > 1$ and $m_n^{\mathrm{I}}(0) = 0$ for all n. This system may be solved using standard matrix methods, giving the solution as a sum of exponential functions.

2. Decomposition using the gain-free solution and polynomial basis functions

Here we apply the decomposition described in Sec. IV B. For Couette flow, the gain-free solution in Eq. (44) becomes

$$\tilde{h}_{\mathrm{gf}}(c_x,c_y,y) = \begin{cases} 2Uc_x\exp\left(-\frac{i\theta-1}{\mathrm{Kn}c_y}(1-y)\right), & c_y < 0 \\ 0, & c_y > 0. \end{cases} \tag{56}$$

This expression is combined with a polynomial trial function, giving

$$\hat{h} = \hat{h}_1 + \tilde{h}_{\mathrm{gf}}, \tag{57}$$

where $\hat{h}_1$ is of the same polynomial form specified in Eqs. (48) and (49). To proceed, we largely repeat the procedure of the preceding section, with the pure polynomial trial function [Eqs. (48) and (49)] replaced by the decomposed trial function in Eq. (57). We amend Eq. (51) to include the source term specified in Eq. (46), resulting from the inclusion of $\tilde{h}_{\mathrm{gf}}$ in the trial function. This yields

$$\begin{aligned} M(\hat{h}^{\mathrm{II}},\hat{h}^{\mathrm{I}}) = &\int_{c_y<0}\hat{h}_1^{\mathrm{II}}(\mathbf{c})\left\{-\mathrm{Kn}c_y\frac{\partial}{\partial y}\hat{h}_1^{\mathrm{I}}(-\mathbf{c}) - L^{\mathrm{I}}[\hat{h}_1(-\mathbf{c})] - i\theta\hat{h}_1^{\mathrm{I}}(-\mathbf{c}) + 2\tilde{h}_{\mathrm{gf}}^{\mathrm{eq}}(-\mathbf{c})\right\}e^{-c^2}d\mathbf{c} \\ &+ \int_{c_y>0}\hat{h}_1^{\mathrm{I}}(\mathbf{c})\left\{-\mathrm{Kn}c_y\frac{\partial}{\partial y}\hat{h}_1^{\mathrm{II}}(-\mathbf{c}) - L^{\mathrm{II}}[\hat{h}_1(-\mathbf{c})] - i\theta\hat{h}_1^{\mathrm{II}}(-\mathbf{c}) + 2\tilde{h}_{\mathrm{gf}}^{\mathrm{eq}}(-\mathbf{c})\right\}e^{-c^2}d\mathbf{c}. \end{aligned} \tag{58}$$

As discussed above, the source term is derived by inserting $\tilde{h} = \tilde{h}_{\mathrm{gf}}$ into Eq. (26), followed by Eq. (25). For Couette flow this gives

$$\tilde{h}_{\mathrm{gf}}^{\mathrm{eq}}(-\mathbf{c}) = -2c_x\tilde{u}_{\mathrm{gf},x}, \tag{59}$$

where

$$\tilde{u}_{\mathrm{gf},x} = \frac{1}{\pi^{3/2}} \int_{c_{y,1}<0} c_{y,1} \tilde{h}_{\mathrm{gf}}(\mathbf{c}_1) e^{-c_1^2} d\mathbf{c}_1. \tag{60}$$

This is the bulk velocity due to the gain-free solution, which may be expressed using the Meijer G function [37]

$$\tilde{u}_{\mathrm{gf},x} = U \frac{(y-1)(i\theta+1)}{4\pi \mathrm{Kn}} G^{0,3}_{3,0}\left(-1/2,0,0 \middle| -\frac{(1-y)^2(i+\theta)^2}{4\mathrm{Kn}^2} \right). \tag{61}$$

As in Sec. V A 1, the integrand M is inserted into Eq. (41) to obtain the Euler-Lagrange equations, the solution of which gives m_n^{I} and m_n^{II}. These functions specify $\hat{h}_1$ via Eq. (32). Note that the Couette flow boundary conditions in Eq. (47) have been applied to the gain-free solution (56). We therefore solve for m_n^{I} and m_n^{II} using homogeneous boundary conditions.

In Fig. 4 we compare results obtained by implementing trial functions that use (i) the simple polynomial expansion in Eq. (49) (derived in the preceding section) and (ii) the gain-free solution (57). Convergence in shear stress, as a function of the degrees of freedom in particle velocity space, is shown for four example flows. The numerical results of Ref. [38] are used as a benchmark; see the figure caption for further detail. As expected, including the gain-free solution in the trial function strongly enhances accuracy for the two most rarefied cases [Figs. 4(a) and 4(b)], with the difference decreasing as the near continuum limit is approached [Fig. 4(d)].

Finally, Fig. 5 shows flow profiles resulting from trial functions that incorporate the simple polynomials given by Eq. (49) and the gain-free solution (57). Once again these are compared to the results given in Ref. [38]. In each of the highly rarefied examples, instabilities arise when a simple polynomial trial function is used, whereas the trial function incorporating the gain-free solution accurately captures the entire flow field.

3. Approximate analytical solutions

Applying the variational approach to one-dimensional problems can produce equations that are analytically tractable when N is sufficiently small. Here we apply the methods in Secs. V A 1 and V A 2 to derive simple expressions approximating the solution for oscillatory Couette flow.

a. Direct solution using polynomial basis functions. We begin with a trial function consisting of a simple polynomial expansion, as in Sec. V A 1. Setting $N = 1$ yields

$$\tilde{h}(c_x,c_y,y) = c_x U \times \begin{cases} \dfrac{2\sinh\left(\sqrt{\pi} y \frac{\zeta}{\mathrm{Kn}}\right)}{2\zeta\cosh\left(\sqrt{\pi}\frac{\zeta}{\mathrm{Kn}}\right)+(1+2i\theta)\sinh\left(\sqrt{\pi}\frac{\zeta}{\mathrm{Kn}}\right)}, & c_y < 0 \\ \dfrac{4\zeta\cosh\left(\sqrt{\pi} y \frac{\zeta}{\mathrm{Kn}}\right)+2(1+2i\theta)\sinh\left(\sqrt{\pi} y \frac{\zeta}{\mathrm{Kn}}\right)}{2\zeta\cosh\left(\sqrt{\pi}\frac{\zeta}{\mathrm{Kn}}\right)+(1+2i\theta)\sinh(\sqrt{\pi}\frac{\zeta}{\mathrm{Kn}})}, & c_y > 0, \end{cases} \tag{62}$$

where $\zeta = \sqrt{\theta(i-\theta)}$, whose real and imaginary parts are both positive. The scaled bulk velocity follows from Eq. (54),

$$\tilde{u}_x = U \frac{\zeta\cosh\left(\sqrt{\pi} y \frac{\zeta}{\mathrm{Kn}}\right) + (1+i\theta)\sinh\left(\sqrt{\pi} y \frac{\zeta}{\mathrm{Kn}}\right)}{2\zeta\cosh\left(\sqrt{\pi}\frac{\zeta}{\mathrm{Kn}}\right) + (1+2i\theta)\sinh\left(\sqrt{\pi}\frac{\zeta}{\mathrm{Kn}}\right)}. \tag{63}$$

The shear stress τ_x is obtained using

$$\tilde{\tau}_x = \frac{1}{\pi^{3/2}} \int_{c_{y,1}>0} c_{x,1} c_{y,1} \hat{h}^{\mathrm{I}}(\mathbf{c}_1) e^{-c_1^2} d\mathbf{c}_1 + \frac{1}{\pi^{3/2}} \int_{c_{y,1}<0} c_x c_{y,1} \hat{h}^{\mathrm{II}}(\mathbf{c}_1) e^{-c_1^2} d\mathbf{c}_1, \tag{64}$$

resulting in

$$\tilde{\tau}_x = U \frac{\zeta\cosh\left(\sqrt{\pi} y \frac{\zeta}{\mathrm{Kn}}\right) + i\theta\sinh\left(\sqrt{\pi} y \frac{\zeta}{\mathrm{Kn}}\right)}{2\sqrt{\pi}\zeta\cosh\left(\sqrt{\pi}\frac{\zeta}{\mathrm{Kn}}\right) + (1+2i\theta)\sqrt{\pi}\sinh\left(\sqrt{\pi}\frac{\zeta}{\mathrm{Kn}}\right)}. \tag{65}$$

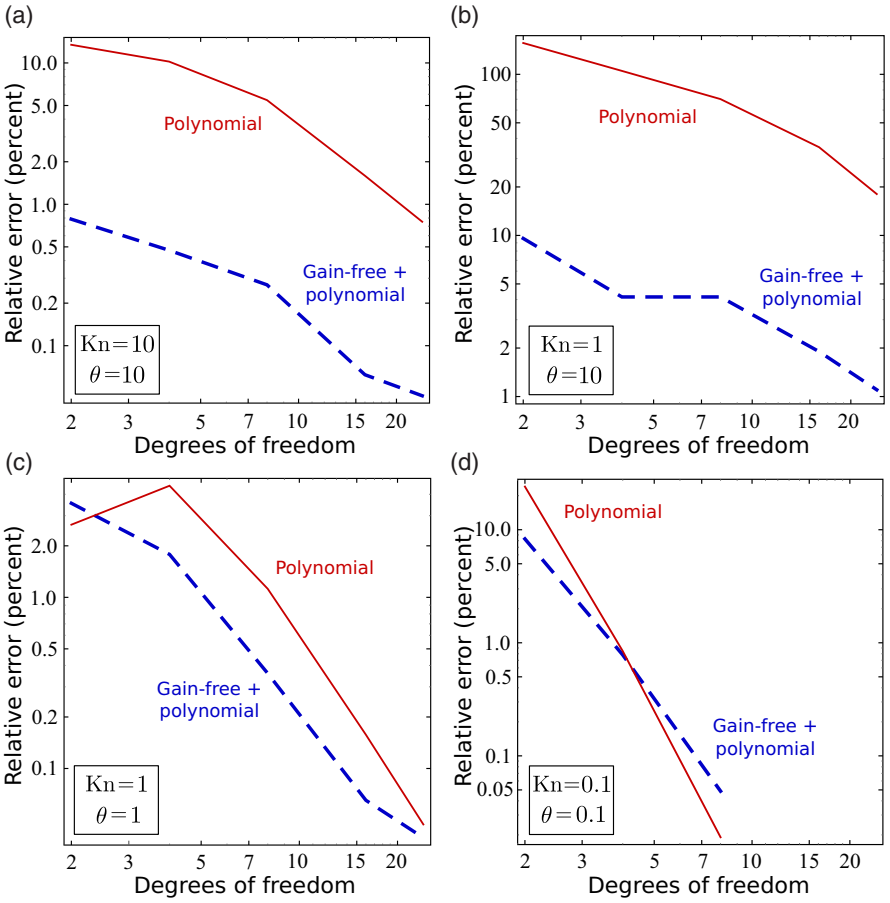

FIG. 4. Oscillatory Couette flow: convergence comparison of the two different trial functions. The solid red lines are for a simple polynomial expansion in particle velocity space [Eq. (49)], where the degrees of freedom listed are specified by $2N$. The dashed blue lines are for trial functions of the form in Eq. (57), which incorporates a polynomial expansion with $2N$ degrees of freedom plus the gain-free solution. The error shown corresponds to that of the shear stress's magnitude, averaged over the entire spatial domain. It is calculated using the high-accuracy solutions of Ref. [38] as benchmarks.

In Fig. 6(a) the bulk velocity field given by Eq. (63) is shown for a range of flow parameters and compared to exact results taken from Ref. [38]. The approximation performs reasonably well for low values of Kn and θ, but becomes inaccurate as rarefaction increases. In Table I(a) the error in shear stress on the oscillating boundary is shown. Once again the results of Ref. [38] are used as a benchmark. The approximation performs well for large Kn and θ, with accuracy decreasing as the continuum limit is approached.

The observation that the shear stress at the oscillating boundary is accurate for highly rarefied flows is unsurprising because the free molecular solution at that position depends only on the boundary condition itself. This is evident by solving the free molecular Boltzmann equation (42), giving

$$\tilde{h}_{\mathrm{fm}}(c_x,c_y,y) = \begin{cases} 2Uc_x \exp\left(-\frac{i\alpha}{c_y}(1-y)\right), & c_y < 0 \\ 0, & c_y > 0, \end{cases} \tag{66}$$

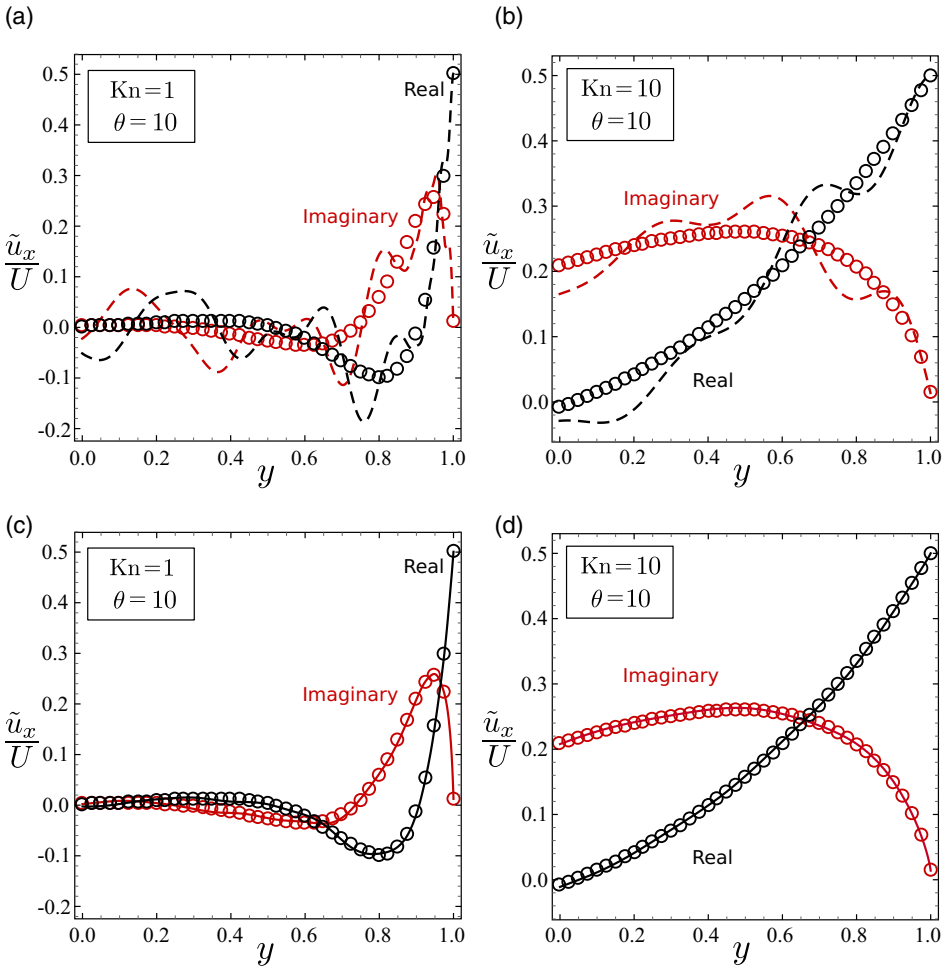

FIG. 5. Oscillatory Couette flow. Bulk velocity profiles for are shown for two highly rarefied flows: (a) and (b) the simple polynomial trial function (49) (dashed lines) and (c) and (d) the trial function incorporating the gain-free solution (57) (solid lines). Open circles denote the high-accuracy numerical solutions of Ref. [38]. In each case, variational solutions using 16 degrees of freedom from Fig. 4 are shown. Instabilities are clearly visible when using a simple polynomial trial function, whereas the trial function incorporating the gain-free solution accurately matches the true solution. [The effect of these instabilities is similar to instabilities seen in other direct numerical solutions of the frequency-domain Boltzmann equation for strongly nonequilibrium (highly rarefied) flows, e.g., see Ref. [39]. In the continuum limit, such oscillations in Eq. (44) are obviously reduced and the function decays exponentially from the boundary. Inclusion of the discontinuous and strongly oscillatory gain-free solution, which arises naturally in highly rarefied flows, can enhance the convergence of solution methods for the Boltzmann equation [36].]

where $\alpha \equiv \theta/\mathrm{Kn}$ is the free molecular parameter. Note that Eq. (66) is derived using the method of characteristics, as described in Sec. IV B. By setting $y = 1$, we observe that the solution is specified entirely by the boundary conditions (55). Because the variational procedure described above is constructed to satisfy the boundary conditions, it exactly captures this case; this is the reason for the high accuracy in shear stress displayed for large Kn and θ [see Table I(a)]. This effect is also

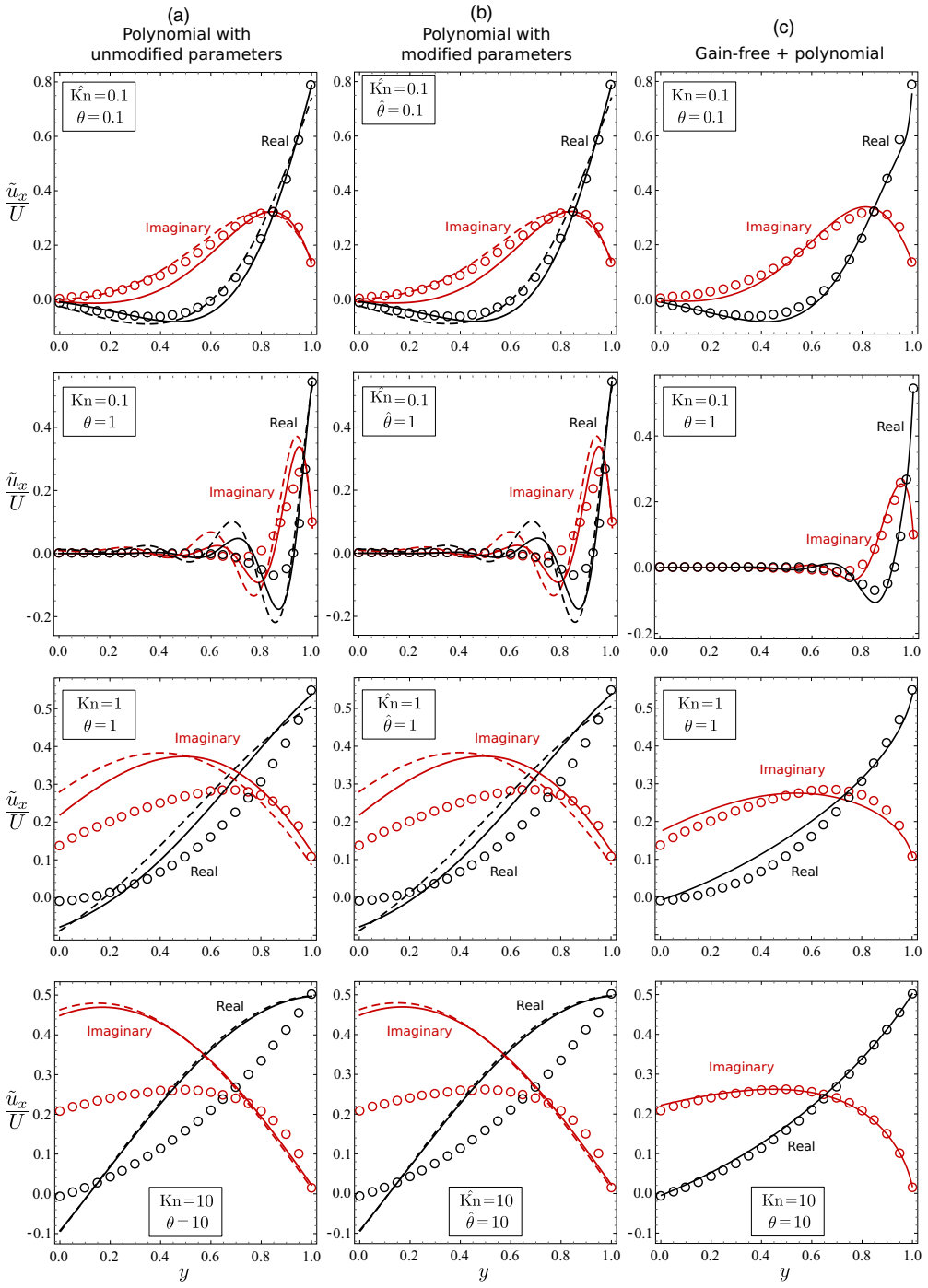

FIG. 6. Oscillatory Couette flow: bulk velocity profiles for a range of Kn and θ values. (a) Solid lines show the approximate analytical solutions obtained using the variational method of Sec. IV, with an $N = 1$ polynomial trial function, i.e., Eq. (63). (b) Solid lines show Eq. (71), which uses the heuristic replacement rule. (c) Solid lines show the approximate solutions where the trial function incorporates the gain-free solution (75). Open circles denote high-accuracy numerical solutions of Ref. [38].

TABLE I. Oscillatory Couette flow. The percentage error in the absolute shear stress on the oscillating boundary is shown. The column headings give the error when the shear stress is calculated using an approximate analytical formula that makes use of an $N = 1$ polynomial basis. (a) Equation (65) is used. (b) Equation (72), which employs the heuristic replacement rule, is used. (c) Error when shear stress is calculated using the formula which incorporates the gain-free solution (76). Errors are calculated for all values of Kn and θ for which accurate benchmark solutions are available in Ref. [38].

	θ			
Kn	0.1	1	10	100
	(a) Polynomial trial function with unmodified parameters			
0.1	13	2.3	0.031	
1	20	0.97	0.30	0.020
10	0.79	1.4	1.0	0.16
	(b) Polynomial trial function with modified parameters			
0.1	3.3	1.5	0.024	
1	5.1	4.7	0.43	0.024
10	2.2	1.5	0.8	0.093
	(c) Gain-free plus polynomial trial function			
0.1	3.3	1.4	0.024	
1	1.1	0.031	0.0029	0.00096
10	0.017	0.46	0.27	0.00066

apparent in the bottom two plots in Fig. 6(a). Although the overall accuracy is poor, the bulk velocity is matched very well at the oscillating boundary $y = 1$.

The poor accuracy in shear stress observed at low Knudsen number (seen in the $\mathrm{Kn} = 0.1$ and $\theta = 0.1$ case) occurs as, approaching the continuum limit, viscous effects arise from the $n = 2$ term in the polynomial expansion given by Eq. (49). In other words, an $N = 2$ expansion will yield a much better approximation of the shear stress; this is evident in the results of Sec. V B. Interestingly, excellent near-continuum results may be obtained, for Couette flow, using an $N = 1$ expansion combined with the rescaling of the flow parameters described in the next section.

b. Direct solution using polynomial basis functions, with modified flow parameters. Here we demonstrate an *ad hoc* approach which produces improved formulas in the case of oscillatory Couette flow. To analyze the above results in the continuum limit we introduce the Stokes parameter $\beta \equiv \theta/\mathrm{Kn}^2$ [40]. The continuum limit is formally recovered by taking $\mathrm{Kn} \to 0$ and $\theta \to 0$ along this path. For the bulk velocity solution given by Eq. (63), we find

$$\tilde{u}_x = U \frac{\sinh(\sqrt{\pi i \beta}\, y)}{\sinh(\sqrt{\pi i \beta})}. \tag{67}$$

This differs from the true solution [38], which is found by solving the Stokes equations directly,

$$\tilde{u}_{\mathrm{S},x} = U \frac{\sinh(\sqrt{2i\beta}\, y)}{\sinh(\sqrt{2i\beta})}, \tag{68}$$

where the subscript S refers to the Stokes solution. Similarly, taking the continuum limit in the shear stress formula given by Eq. (65) yields

$$\tilde{\tau}_x = U\,\mathrm{Kn}\sqrt{\frac{i\beta}{\pi}}\frac{\cosh(\sqrt{\pi i \beta}\, y)}{\sinh(\sqrt{\pi i \beta})}, \tag{69}$$

which once again differs from the true solution

$$\tilde{\tau}_{S,x} = U\,\mathrm{Kn}\sqrt{\frac{i\beta}{2}}\frac{\cosh(\sqrt{2i\beta}y)}{\sinh(\sqrt{2i\beta})}. \tag{70}$$

The error in Eqs. (67) and (69) arises because they are derived using the $N = 1$ polynomial expansion, containing only the single term c_y. The $N = 2$ trial function, containing $c_x c_y$, is required to capture the correct result in the continuum limit (68) and (70). In this latter case, it is possible (in principle) to derive a formula since the matrix eigenvalues and vectors may be found analytically. However, this is difficult for Couette flow due to the presence of two solid walls; this approach is more practical for Stokes' second problem, which is discussed in Sec. V B.

Interestingly, the solutions in Eqs. (67) and (69) match Eqs. (68) and (70) if we replace the Stokes parameter using $\beta \to (2/\pi)\beta$ or equivalently $\mathrm{Kn} \to (\pi/2)\mathrm{Kn}$ and $\theta \to (\pi/2)\theta$. Applying this change to Eqs. (63) and (65) yields

$$\tilde{u}_x = U\frac{\sqrt{\pi}\hat{\zeta}\cosh\left(y\frac{\hat{\zeta}}{\mathrm{Kn}}\right) + (2 + i\pi\theta)\sinh\left(y\frac{\hat{\zeta}}{\mathrm{Kn}}\right)}{2\sqrt{\pi}\hat{\zeta}\cosh\left(\frac{\hat{\zeta}}{\mathrm{Kn}}\right) + 2(1 + i\pi\theta)\sinh\left(\frac{\hat{\zeta}}{\mathrm{Kn}}\right)}, \tag{71}$$

$$\tilde{\tau}_x = U\frac{\hat{\zeta}\cosh\left(y\frac{\hat{\zeta}}{\mathrm{Kn}}\right) + i\sqrt{\pi}\theta\sinh\left(y\frac{\hat{\zeta}}{\mathrm{Kn}}\right)}{2\sqrt{\pi}\hat{\zeta}\cosh\left(\frac{\hat{\zeta}}{\mathrm{Kn}}\right) + 2(1 + i\pi\theta)\sqrt{\pi}\sinh\left(\frac{\hat{\zeta}}{\mathrm{Kn}}\right)}, \tag{72}$$

where $\hat{\zeta} = \sqrt{\theta(2i - \pi\theta)}$. Using these heuristically modified parameters gives the correct bulk velocity and shear stress in the continuum limit and greatly improves accuracy for low Kn and θ. Interestingly, only a modest reduction in accuracy is seen for intermediate values of Kn and θ, and almost no difference to Eqs. (67) and (69) is observed for highly rarefied flows. This is illustrated in Fig. 6(b), where a range of bulk velocity profiles, given by Eq. (71), are again compared to the exact solutions. The observed invariance in the large Kn and θ results, under this heuristic modification, follows from the fact that the free molecular parameter is unchanged. In Table I(b) the error in the shear stress at the oscillating boundary, given by Eq. (72), is shown. The heuristically modified formulas, which match the continuum limit, display a marked improvement in accuracy.

c. Decomposition using the gain-free solution and polynomial basis functions. Incorporating the gain-free solution, as in Sec. V A 2, and setting $N = 1$ gives

$$\tilde{h}_1(c_x, c_y, y) = c_x\begin{cases}\tilde{h}_1^{\mathrm{II}}, & c_y < 0\\ \tilde{h}_1^{\mathrm{I}}, & c_y > 0,\end{cases} \tag{73}$$

where

$$\begin{aligned}\tilde{h}_1^{\mathrm{I}} = \frac{U}{2\zeta}\Bigg\{&A_+(0,y)\left[2\zeta\cosh\left(\frac{\sqrt{\pi}\zeta}{\mathrm{Kn}}y\right) - (1 + 2i\theta)\sinh\left(\frac{\sqrt{\pi}\zeta}{\mathrm{Kn}}y\right)\right]\\ &+\left(A_+(0,1)\frac{\sinh\left(\frac{\sqrt{\pi}\zeta}{\mathrm{Kn}}\right)}{2\zeta\cosh\left(\frac{\sqrt{\pi}\zeta}{\mathrm{Kn}}\right) + (1 + 2i\theta)\sinh\left(\frac{\sqrt{\pi}\zeta}{\mathrm{Kn}}\right)} - A_-(y,1)\right)\sinh\left(\frac{\sqrt{\pi}\zeta}{\mathrm{Kn}}y\right)\Bigg\},\\ \tilde{h}_1^{\mathrm{II}} = \frac{U}{2\zeta}\Bigg\{&\left(A_+(0,1)\frac{\sinh\left(\frac{\sqrt{\pi}\zeta}{\mathrm{Kn}}\right)}{2\zeta\cosh\left(\frac{\sqrt{\pi}\zeta}{\mathrm{Kn}}\right) + (1 + 2i\theta)\sinh\left(\frac{\sqrt{\pi}\zeta}{\mathrm{Kn}}\right)} - A_-(y,1)\right)\\ &\times\left[2\zeta\cosh\left(\frac{\sqrt{\pi}\zeta}{\mathrm{Kn}}y\right) - (1 + 2i\theta)\sinh\left(\frac{\sqrt{\pi}\zeta}{\mathrm{Kn}}y\right)\right] + A_+(0,y)\sinh\left(\frac{\sqrt{\pi}\zeta}{\mathrm{Kn}}y\right)\Bigg\},\end{aligned} \tag{74}$$

with

$$A_\pm(a,b) = \frac{2\sqrt{\pi}}{\mathrm{Kn}\zeta}\int_a^b \tilde{u}_{\mathrm{gf},x}(y_1)\left\{\pm\zeta\cosh\left(\frac{\sqrt{\pi}\zeta}{\mathrm{Kn}}y_1\right) + (1 + i\theta)\sinh\left(\frac{\sqrt{\pi}\zeta}{\mathrm{Kn}}y_1\right)\right\}dy_1.$$

The bulk velocity incorporating the gain-free solution is given by

$$\tilde{u}_x = \tilde{u}_{\mathrm{gf},x} + \frac{\tilde{h}_1^{\mathrm{I}}}{4} + \frac{\tilde{h}_1^{\mathrm{II}}}{4}, \tag{75}$$

where $\tilde{u}_{\mathrm{gf},x}$ is given in Eq. (61), and the shear stress is

$$\tilde{\tau}_x = \tilde{\tau}_{\mathrm{gf},x} + \frac{\tilde{h}^{\mathrm{I}}}{4\sqrt{\pi}} - \frac{\tilde{h}^{\mathrm{II}}}{4\sqrt{\pi}}, \tag{76}$$

where

$$\tilde{\tau}_{\mathrm{gf},x} = -U\frac{(y-1)^2(\theta-i)}{8\pi\,\mathrm{Kn}} G^{0,3}_{3,0}\left(_{-1,-1/2,0}\middle| -\frac{(1-y)^2(\theta-i)^2}{4\mathrm{Kn}^2}\right). \tag{77}$$

Figure 6(c) shows the approximate velocity fields given by Eq. (75), for a range of Knudsen numbers and scaled oscillation frequencies; Ref. [38] is again used for comparison. For moderate to highly rarefied flows $\mathrm{Kn} > 0.1$ and $\theta > 0.1$, the approximation that incorporates the gain-free solution is more accurate than the approximation given by Eq. (63), shown in Fig. 6(a). Unsurprisingly, the difference in accuracy is enhanced with increasing rarefaction.

In Table I(c) the error in the shear stress at the oscillating boundary is given. We see that Eq. (76) provides an excellent estimate of the shear stress across a wide range of Knudsen numbers and oscillation frequencies. Again, this approximation exhibits smaller error compared to the simple polynomial solution (65) in the region $\mathrm{Kn} > 0.1$ and $\theta > 0.1$.

It is difficult to formally take the continuum limit for Eqs. (75) and (76); however, numerical analysis indicates that the relative error in both expressions rapidly increases as $\mathrm{Kn} \to 0$ and $\theta \to 0$, suggesting that these approximations should only be applied when $\mathrm{Kn} \geqslant 0.1$ and $\theta \geqslant 0.1$. This contrasts with Eqs. (71) and (72), which are exact in the continuum limit.

4. Comparison to steady (near-continuum) slip solution

Polynomial solutions of the type studied in Sec. V A 1 are most accurate for slightly rarefied flows (near continuum). They may therefore be compared to Navier-Stokes solutions obtained using slip boundary conditions, which are also derived for slightly rarefied flows. For simplicity, we restrict our analysis to the steady case ($\theta = 0$); however, these observations apply equally to the oscillatory flows of the previous sections.

Continuum equations may be obtained from the Boltzmann equation via a Hilbert expansion in the asymptotic limit of low Knudsen number. This process is detailed in Refs. [12,41] (and Ref. [42] for unsteady flows). At leading order, the Stokes equations for creeping flow are obtained, with $O(\mathrm{Kn})$ corrections occurring at the solid boundaries; these are the first-order slip boundary conditions. For steady Couette flow, the Stokes equations reduce to

$$\frac{\partial^2 u_x}{\partial y^2} = 0. \tag{78}$$

We henceforth omit the subscript x and employ the notation u_0 to describe the (leading-order) continuum solution to Eq. (78). The $O(\mathrm{Kn})$ correction obtained using the slip boundary condition is designated u_1 and thus the complete slip solution is $u_s = u_0 + \mathrm{Kn}u_1 + O(\mathrm{Kn}^2)$. The required boundary conditions at each solid wall are formally

$$u_s(0) = \sigma\,\mathrm{Kn}\frac{\partial u_0}{\partial y}\bigg|_{y=0}, \quad u_s(1) = U - \sigma\,\mathrm{Kn}\frac{\partial u_0}{\partial y}\bigg|_{y=1}, \tag{79}$$

where σ is the first-order slip coefficient. This is derived for steady flow in Ref. [41] and for oscillatory flow in Ref. [42]. In each case fully diffuse boundary conditions are assumed, for which $\sigma = 1.0162$.

In practice, the following formulas are often used (they are correct to identical order in Kn):

$$u_s(0) = \sigma \mathrm{Kn} \left.\frac{\partial u_s}{\partial y}\right|_{y=0}, \quad u_s(1) = U - \sigma \mathrm{Kn} \left.\frac{\partial u_s}{\partial y}\right|_{y=1}. \tag{80}$$

This yields a solution which matches the one obtained using the boundary conditions in Eq. (79), to $O(\mathrm{Kn})$. The solution to Eqs. (78) and (80) is

$$u_s(y) = \frac{y + \sigma\ \mathrm{Kn}}{1 + 2\sigma\ \mathrm{Kn}}, \tag{81}$$

which may be expanded

$$u_s(y) = u_0(y) + \ \mathrm{Kn} u_1(y)\ + O(\mathrm{Kn}^2), \tag{82}$$

where $u_0(y) = y$ and $u_1(y) = \sigma y$. Equation (82) is the solution obtained when the formal boundary conditions in Eq. (79) are used.

We now apply the simple polynomial approach of Sec. V A 1, with $\theta = 0$, using trial functions of the form in Eqs. (48) and (49). The resulting system of equations is

$$\frac{\partial}{\partial y}\hat{\mathbf{h}} = \frac{1}{\mathrm{Kn}}\mathbf{A}\hat{\mathbf{h}}, \tag{83}$$

where

$$\hat{\mathbf{h}} = \begin{bmatrix} \tilde{v}_1(y) \\ \vdots \\ \tilde{v}_N(y) \\ \tilde{b}_1(y) \\ \vdots \\ \tilde{b}_N(y) \end{bmatrix} \tag{84}$$

and $\mathbf{A}$ is defined separately for each value of N used below. As mentioned previously, this system may be solved using standard matrix methods. For steady flows a fully analytical solution is possible up to $N = 3$; however, in practice, this is difficult for $N > 2$. We note that, as per Eq. (83), the dependence on Knudsen number may be factored out of the matrix $\mathbf{A}$, allowing the eigenvalues to be determined numerically for all Kn. This greatly simplifies analysis for $N > 2$, although solutions become more complex as N increases.

For $N = 1$ the matrix $\mathbf{A}$ is

$$\mathbf{A} = \frac{\sqrt{\pi}}{2}\begin{bmatrix} -1 & 1 \\ -1 & 1 \end{bmatrix}. \tag{85}$$

The solution to Eq. (83) gives

$$u(y) = \frac{y + \sigma_1 \mathrm{Kn}}{1 + 2\sigma_1 \mathrm{Kn}}, \tag{86}$$

where $\sigma_1 = 1/\sqrt{\pi}$. This is the leading-order solution in the particle velocity coordinate c_y. It is of identical form to Eq. (81), but with a slip coefficient $\sigma_1 = 1/\sqrt{\pi} = 0.5642$ rather than $\sigma = 1.0162$. The subscript 1 is used to denote the value arising from the $N = 1$ solution, and similarly for larger values of N.

For $N = 2$ the matrix $\mathbf{A}$ is

$$\mathbf{A} = \frac{1}{\sqrt{\pi}(4-\pi)}\begin{bmatrix} -\pi & (-3+\pi)\sqrt{\pi} & \pi & -\sqrt{\pi} \\ (-2+\pi)\sqrt{\pi} & 2-\pi & (2-\pi)\sqrt{\pi} & -2+\pi \\ -\pi & -\sqrt{\pi} & \pi & (-3+\pi)\sqrt{\pi} \\ (2-\pi)\sqrt{\pi} & 2-\pi & (-2+\pi)\sqrt{\pi} & -2+\pi \end{bmatrix} \tag{87}$$

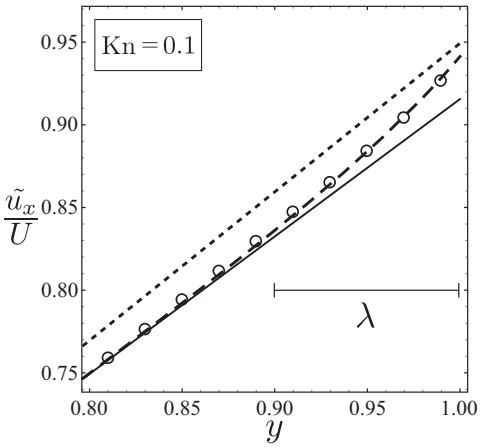

FIG. 7. Steady Couette flow: bulk velocity profile near the moving plate for Kn = 0.1 (and $\theta = 0$). The slip solution correct to $O(\mathrm{Kn})$ is the solid straight line, while the $N = 1$ and $N = 2$ variational solutions are the dotted and dashed curves, respectively. The open circles are the exact solution obtained using the Monte Carlo method of Refs. [43,44]. As expected, the slip solution (solid line) matches the flow away from the wall, but does not account for the Knudsen layer near the wall. Conversely, the $N = 1$ solution (dotted curve) accurately approximates the true boundary condition but is poor away from the wall. The $N = 2$ solution (dashed curve) provides a good approximation over the entire flow domain.

and the solution to Eq. (83) gives

$$u(y) = \frac{\exp\left(\frac{\eta}{\mathrm{Kn}}\right)\mathrm{Kn}(\pi-4) + \beta_{-}\mathrm{Kn}\left\{\exp\left(\frac{(2-y)\eta}{\mathrm{Kn}}\right) - \exp\left(\frac{(1+y)\eta}{\mathrm{Kn}}\right)\right\}}{4\exp\left(\frac{\eta}{\mathrm{Kn}}\right)\mathrm{Kn}(\pi-4) + \exp\left(\frac{2\eta}{\mathrm{Kn}}\right)(2\alpha_{-}\mathrm{Kn} - \gamma_{-}) + 2\alpha_{+}\mathrm{Kn} + \gamma_{+}}$$
$$+ \frac{\beta_{+}\mathrm{Kn}\left\{\exp\left(\frac{\eta}{\mathrm{Kn}}\right) - \exp\left(\frac{y\eta}{\mathrm{Kn}}\right)\right\} - \exp\left(\frac{2\eta}{\mathrm{Kn}}\right)\left\{y\gamma_{-} - \alpha_{-}\mathrm{Kn}\right\} + \left\{y\gamma_{+} + \alpha_{+}\mathrm{Kn}\right\}}{4\exp\left(\frac{\eta}{\mathrm{Kn}}\right)\mathrm{Kn}(\pi-4) + \exp\left(\frac{2\eta}{\mathrm{Kn}}\right)(2\alpha_{-}\mathrm{Kn} - \gamma_{-}) + 2\alpha_{+}\mathrm{Kn} + \gamma_{+}}, \quad (88)$$

where

$$\alpha_{\pm} = 4 + \pi \pm 3\sqrt{2\pi}, \quad \beta_{\pm} = \pm 2 + \sqrt{2\pi}, \quad \gamma_{\pm} = 2\sqrt{2} \pm 4\sqrt{\pi} + \sqrt{2}\pi, \quad \eta = \frac{\sqrt{2}(\pi-2)}{(\pi-4)}.$$

Taking the limit $\mathrm{Kn} \to 0$ in Eq. (88) again yields a solution with the form of Eq. (81). In this case, the slip coefficient is $\sigma_2 = \alpha_{+}/\gamma_{+} = 1.0209$. A very good approximation to the true slip coefficient ($\sigma = 1.0162$) and the $O(\mathrm{Kn})$ solution is therefore obtained using a low-order approximation in particle velocity space.

For $N = 3$ the eigenvalues for $\mathbf{A}$ in this case are found numerically, as described above. The matrix $\mathbf{A}$ and function $u(y)$ are too complex to reproduce here; however, using a procedure similar to that for $N = 2$ gives a solution of identical form to Eq. (81), with a slip coefficient of $\sigma_3 = 1.0171$.

Figure 7 compares flow fields obtained from the complete $N = 1$ [Eq. (86)] and $N = 2$ [Eq. (88)] solutions, that due to the slip solution in Eq. (81), and a direct solution of the Boltzmann equation using the Monte Carlo method of Refs. [43,44]. While closely matching the slip result in the body of the flow, the $N = 2$ solution provides a better approximation to the true velocity field in the Knudsen layer.

B. Stokes' second problem

In this section we demonstrate two approaches that yield approximate solutions for Stokes' second problem. Each of these approaches makes use of an $N = 2$ trial function and therefore provides the

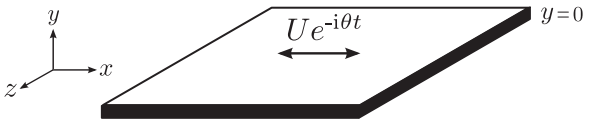

FIG. 8. Schematic of Stokes' second problem showing the coordinate system.

correct solution in the continuum limit. First, we derive a simple system of ordinary differential equations that incorporates the gain-free solution discussed in Sec. IV B. This system is easily solved using standard numerical techniques. Second, we find an analytical solution using a simple polynomial trial function in the same manner as in Sec. V A 3 a. In the case of Stokes' second problem, this is possible for $N = 2$. As the resulting solution is impracticably large, we provide a formula which further approximates the shear stress at the surface of the oscillating plate (see the Supplemental Material in [45]).

The spatial domain is bounded at $y = 0$ by a wall oscillating longitudinally along the x axis with amplitude U and angular frequency θ. The domain is unbounded in the x, z, and positive y directions (see Fig. 8). The wall at $y = 0$ is diffusely reflecting, with the boundary condition following from Eq. (15) and given by

$$\tilde{h}^+(0) = 2Uc_x, \quad c_y > 0. \tag{89}$$

The gas far from the wall ($y \to \infty$) is in the global (quiescent) equilibrium state, which is implemented numerically by applying the open boundary condition at $y = Y_b$,

$$\tilde{h}^+(Y_b) = 0, \quad c_y < 0, \tag{90}$$

where Y_b is increased systematically until it has no appreciable effect on the solution.

Because this flow lacks any geometric scale, the length scale is chosen to be the most probable distance traveled by a gas particle in a single oscillation period, i.e., $l = \sqrt{2RT_0}/\omega$. Applying this new length scale to Eq. (23) gives

$$-i\theta\tilde{h} + \theta\mathbf{c} \cdot \frac{\partial \tilde{h}}{\partial \mathbf{x}} = L[\tilde{h}], \tag{91}$$

where the source term s is zero for Stokes' second problem. The lack of a geometric length scale causes the degree of rarefaction to be governed exclusively by the scaled oscillation frequency, with the flow becoming more rarefied for larger θ.

1. Simple equations obtained using the gain-free methodology

In Ref. [46], Eq. (91) is solved using both finite-difference and integro-moment [47] methods, with the shear stress at the oscillating boundary calculated for a range of θ values.[3] Here we employ the variational method of Sec. IV B, which incorporates the gain-free solution, to derive a simple system of ordinary differential equations. These equations are easily solved to obtain approximate solutions for arbitrary θ.

As before, we begin with the gain-free equation

$$\theta\mathbf{c} \cdot \frac{\partial \tilde{h}}{\partial \mathbf{x}} = (i\theta - 1)\tilde{h}, \tag{92}$$

[3]The reader is cautioned that in Ref. [46] the definition of θ is the reciprocal of that used in this article, i.e., $\theta = \nu/\omega$.

which yields the solution

$$\tilde{h}_{\mathrm{gf}}(c_x,c_y,y)=\begin{cases}0, & c_y<0\\ 2Uc_x\exp\left(\frac{i\theta-1}{\theta c_y}y\right), & c_y>0,\end{cases} \tag{93}$$

where we have applied the boundary condition in Eq. (89). From Eq. (45) we then obtain

$$\theta\mathbf{c}\cdot\frac{\partial\tilde{h}_1}{\partial\mathbf{x}}=(i\theta\tilde{h}_1-1)+\tilde{h}_1^{\mathrm{eq}}+\tilde{h}_{\mathrm{gf}}^{\mathrm{eq}}. \tag{94}$$

Following the same procedure as Sec. V A 2, the functional in Eq. (41) becomes

$$\begin{aligned}M=&\int_{c_y<0}\hat{h}_1^{\mathrm{II}}(\mathbf{c})\left\{-\theta c_y\frac{\partial}{\partial y}\hat{h}_1^{\mathrm{I}}(-\mathbf{c})-L^{\mathrm{I}}[\hat{h}_1(-\mathbf{c})]-i\theta\hat{h}_1^{\mathrm{I}}(-\mathbf{c})+2\tilde{h}_{\mathrm{gf}}^{\mathrm{eq}}(-\mathbf{c})\right\}e^{-c^2}d\mathbf{c}\\&+\int_{c_y>0}\hat{h}_1^{\mathrm{I}}(\mathbf{c})\left\{-\theta c_y\frac{\partial}{\partial y}\hat{h}_1^{\mathrm{II}}(-\mathbf{c})-L^{\mathrm{II}}[\hat{h}_1(-\mathbf{c})]-i\theta\hat{h}_1^{\mathrm{II}}(-\mathbf{c})+2\tilde{h}_{\mathrm{gf}}^{\mathrm{eq}}(-\mathbf{c})\right\}e^{-c^2}d\mathbf{c},\end{aligned} \tag{95}$$

where

$$\tilde{h}_{\mathrm{gf}}^{\mathrm{eq}}(-\mathbf{c})=-2c_x\tilde{u}_{\mathrm{gf},x} \tag{96}$$

and

$$\tilde{u}_{\mathrm{gf},x}=U\frac{y(1-i\theta)}{4\pi\theta}G_{3,0}^{0,3}\left(_{-1/2,0,0}\middle|-\frac{y^2(i+\theta)^2}{4\theta^2}\right). \tag{97}$$

In Sec. V A 3, $\hat{h}^{\mathrm{I}}$ and $\hat{h}^{\mathrm{II}}$ are each specified using a single term to obtain analytically tractable equations. Here we instead use

$$\hat{h}^{\mathrm{I}}=c_xm_1^{\mathrm{I}}(y)+c_xc_ym_2^{\mathrm{I}}(y),\quad \hat{h}^{\mathrm{II}}=c_xm_1^{\mathrm{II}}(y)+c_xc_ym_2^{\mathrm{II}}(y). \tag{98}$$

Combining Eqs. (41), (95), and (98) then gives the required system

$$\frac{\partial}{\partial y}\hat{\mathbf{h}}=\frac{1}{(\pi-4)\theta}\mathbf{A}\hat{\mathbf{h}}+\frac{\tilde{u}_{\mathrm{gf},x}(y)}{(\pi-4)\theta}\mathbf{d}, \tag{99}$$

where

$$\hat{\mathbf{h}}=\begin{bmatrix}m_1^{\mathrm{I}}(y)\\ m_2^{\mathrm{I}}(y)\\ m_1^{\mathrm{II}}(y)\\ m_2^{\mathrm{II}}(y)\end{bmatrix},\quad \mathbf{d}=\begin{bmatrix}-4\sqrt{\pi}\\ 4(\pi-2)\\ 4\sqrt{\pi}\\ 4(\pi-2)\end{bmatrix}, \tag{100}$$

and

$$\mathbf{A}=\begin{bmatrix}\sqrt{\pi}(1-2i\theta) & 3-4i\theta+i\pi(i+\theta) & -\sqrt{\pi} & 1\\ (\pi-2)(2i\theta-1) & \frac{\pi-2}{\sqrt{\pi}} & \pi-2 & \frac{2-\pi}{\sqrt{\pi}}\\ \sqrt{\pi} & 1 & \sqrt{\pi}(2i\theta-1) & 3-4i\theta+i\pi(i+\theta)\\ \pi-2 & \frac{\pi-2}{\sqrt{\pi}} & (2i\theta-1)(\pi-2) & \frac{2-\pi}{\sqrt{\pi}}\end{bmatrix}. \tag{101}$$

These equations are easily solved[4] to obtain an approximate solution to Eq. (91) for arbitrary θ. As discussed in Sec. V A 2, homogeneous boundary conditions are to be used in solving Eq. (99),

[4]We note that the system of equations (99) is essentially transport equations for the individual spectral components of the solution. Where any numerical method with a directional flux of information is used, it should be applied in the direction 'upwind' from the boundary condition for each individual equation.

TABLE II. Stokes' second problem. The percentage error in the magnitude and phase of the shear stress on the oscillating solid wall is shown for three different variational solutions: (a) obtained by numerically solving Eq. (99); (b) results from analytically solving the same system as in (a) but setting $\tilde{u}_{\mathrm{gf},x}(y) = 0$, i.e., the polynomial method (this solution is provided in the *Mathematica* file in [45]); and (c) analytical formula (103) derived by approximating the solution used in (b). Although the italicized percentage errors are large, the absolute error is much less than 0.1, because the phase approaches zero for large θ. Errors are calculated using, as benchmarks, high-accuracy results from the approach of Sec. V A 1 for $\theta \leqslant 1$ and Sec. IV A for $\theta > 1$. These high-accuracy results agree with those of Ref. [46], except for $\theta = 0.02$, where discrepancies of 1.9% in the magnitude and 0.2% in the phase are observed.

	θ						
Parameter	0.02	0.05	0.1	0.2	1	10	100
	(a) Numerical solution to Eq. (99), including the gain-free term						
Magnitude	0.17	0.13	0.039	0.18	0.27	0.0033	0.0025
Phase	0.081	0.26	0.47	0.69	0.91	1.3	1.5
	(b) Analytic solution to Eq. (102), excluding the gain-free term						
Magnitude	0.019	0.33	0.58	0.88	0.52	0.00070	0.013
Phase	0.34	0.62	0.78	0.59	3.1	4.1	4.3
	(c) Approximation of the analytic solution (103)						
Magnitude	0.019	0.33	0.59	0.89	0.034	1.9	0.35
Phase	0.34	0.62	0.79	0.58	2.8	*186*	*154*

because the condition for the moving wall [Eq. (89)] is applied to $\tilde{u}_{\mathrm{gf},x}(y)$. In Table II the error in shear stress at the oscillating boundary is shown for several values of θ. In Fig. 9 several bulk velocity profiles are compared to those obtained using the frequency-domain Monte Carlo approach of Refs. [34,48]; good agreement is obtained for a wide range of θ values.

2. Accurate formula for shear stress at the solid wall using the polynomial approach

Finally, we derive a simple and accurate formula for the shear stress at the solid wall in Stokes' second problem, which may be of value in practice. Setting $\tilde{u}_{\mathrm{gf},x}(y) = 0$ in Eq. (99) yields the system of equations arising from a simple polynomial trial function

$$\frac{\partial}{\partial y}\hat{\mathbf{h}} = \frac{1}{(\pi - 4)\theta}\mathbf{A}\hat{\mathbf{h}}, \tag{102}$$

where $\hat{\mathbf{h}}$ and $\mathbf{A}$ are given by Eqs. (100) and (101). The removal of $\tilde{u}_{\mathrm{gf},x}$ greatly simplifies the application of standard matrix techniques for Stokes' second problem, making it practical to derive an analytical solution. Note that, because we have discarded the gain-free term, the moving wall boundary condition must now be applied to solve these equations. The resulting solution to Eq. (102) is complicated and is provided in a *Mathematica* file in [45]. This solution is valuable because it may be used as the basis for further approximation, giving simple formulas for quantities of interest. For example, the shear stress at the oscillating surface can be well approximated by

$$\tilde{\tau}_{y=0} = \frac{U}{1 + \left(\frac{\theta}{20}\right)^2} S_{2/2}(\theta) + \frac{\left(\frac{\theta}{20}\right)^2}{1 + \left(\frac{\theta}{20}\right)^2} \frac{U}{2\sqrt{\pi}}, \tag{103}$$

where

$$S_{2/2}(\theta) = \frac{0.5(1-i)\sqrt{\theta} - 3.819\,61i\theta - 5.486\,84(1+i)\theta^{3/2} - 3.041\,58\theta^2}{1 + 4.840\,52(1-i)\sqrt{\theta} - 19.4812i\theta - 16.7356(1+i)\theta^{3/2} - 12.326\theta^2}. \tag{104}$$

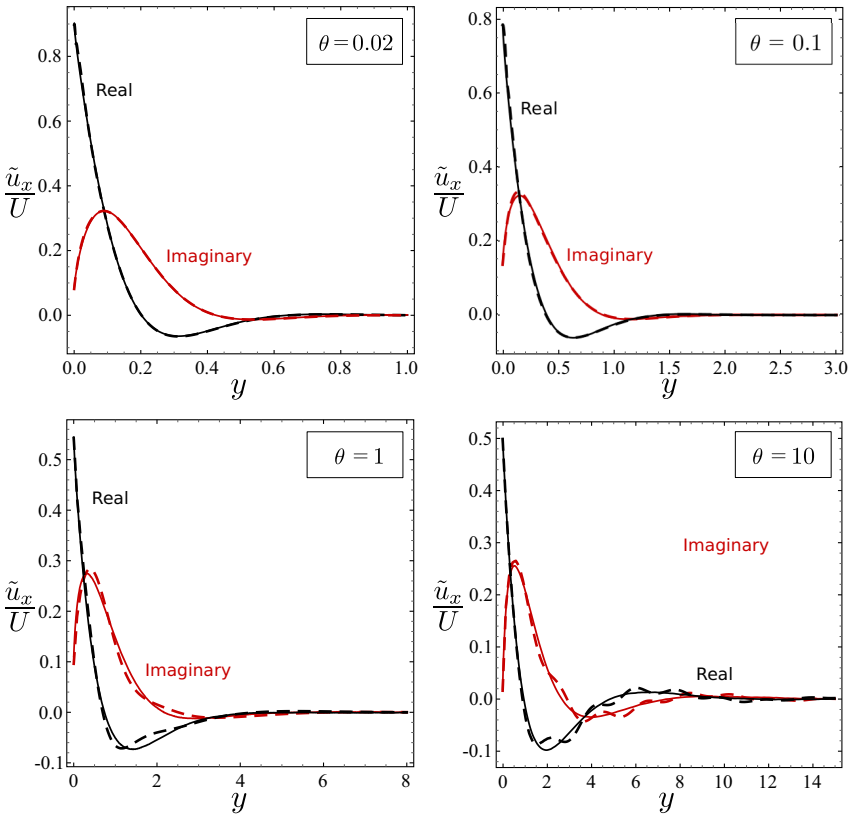

FIG. 9. Stokes' second problem. Bulk velocity profiles are shown as a function of θ values. Solid curves show the frequency-domain Monte Carlo solutions obtained using the method of Refs. [34,48] and dashed curves the variational approximation of Eq. (99), which gives good agreement with the true (Monte Carlo) solution. Note that the oscillations visible in the $\theta = 10$ case are inaccuracies which may be removed by increasing the order of the trial function. They are not a numerical instability of the kind discussed in Sec. IV B and seen in Figs. 5(a) and 5(b).

Equation (103) is derived using several simplifications to (i) make the problem tractable and (ii) obtain a solution that is reasonably concise. First, the system of equations (102) is solved using eigenvectors expanded in θ to third order about $\theta = 0$. The resulting shear stress formula is somewhat simpler than the full solution (shown in the *Mathematica* file in [45]), but is accurate only for $\theta < 1$. This formula is further simplified by taking the order $[2/2]$ Padé approximation, again around $\theta = 0$, giving Eq. (104). This expression remains accurate in the region $\theta < 1$; however, it does not give the correct result as $\theta \to \infty$, due to approximation of the eigenvectors (above) in solving Eq. (102). This is addressed in Eq. (103) by combining the Padé approximant with the $\theta \to \infty$ solution $1/2\sqrt{\pi}$. The combination has been chosen such that the crossover between the low- and high-θ solutions occurs at $\theta = 20$. This value is selected empirically, resulting in an error of less that 2.5% in the shear stress magnitude for all values of θ (see Table II). For comparison, the error exhibited by the complete analytic solution to Eq. (102) is also shown.

VI. CONCLUSION

We have extended Cercignani's variational method, originally formulated for steady flows, to oscillatory flows of the type generated by resonating nanomechanical devices. This was done by

TABLE III. Summary of approximate oscillatory flow solutions derived in this study.

Expansion	Formula	Solution
	Couette flow	
$N = 1$ polynomial expansion using heuristic replacement rule	Bulk velocity (71)	$\tilde{u}_x = U\frac{\sqrt{\pi}\hat{\zeta}\cosh(y\frac{\hat{\zeta}}{\mathrm{Kn}})+(2+i\pi\theta)\sinh(y\frac{\hat{\zeta}}{\mathrm{Kn}})}{2\sqrt{\pi}\hat{\zeta}\cosh(\frac{\hat{\zeta}}{\mathrm{Kn}})+2(1+i\pi\theta)\sinh(\frac{\hat{\zeta}}{\mathrm{Kn}})}$
	Shear stress (72)	$\tilde{\tau}_x = U\frac{\hat{\zeta}\cosh(y\frac{\hat{\zeta}}{\mathrm{Kn}})+i\sqrt{\pi}\theta\sinh(y\frac{\hat{\zeta}}{\mathrm{Kn}})}{2\sqrt{\pi}\hat{\zeta}\cosh(\frac{\hat{\zeta}}{\mathrm{Kn}})+2(1+i\pi\theta)\sqrt{\pi}\sinh(\frac{\hat{\zeta}}{\mathrm{Kn}})}$ where $\hat{\zeta} = \sqrt{\theta(2i-\pi\theta)}$
$N = 1$ polynomial expansion including gain-free term	Bulk velocity (75)	$\tilde{u}_x = \tilde{u}_{\mathrm{gf},x} + \frac{\tilde{h}_1^{\mathrm{I}}}{4} + \frac{\tilde{h}_1^{\mathrm{II}}}{4}$ where $\tilde{u}_{\mathrm{gf},x}, \tilde{h}_1^{\mathrm{I}}$, and $\tilde{h}_1^{\mathrm{II}}$ are specified in Eqs. (61) and (74)
	Shear stress (76)	$\tilde{\tau}_x = \tilde{\tau}_{\mathrm{gf},x} + \frac{\tilde{h}_1^{\mathrm{I}}}{4\sqrt{\pi}} + \frac{\tilde{h}_1^{\mathrm{II}}}{4\sqrt{\pi}}$ where $\tilde{\tau}_{\mathrm{gf},x}, \tilde{h}_1^{\mathrm{I}}$, and $\tilde{h}_1^{\mathrm{II}}$ are specified in Eqs. (77) and (74)
	Stokes' second problem	
$N = 2$ polynomial expansion, approximate analytical solution	Shear stress at oscillating surface Eq. (103)	$\tilde{\tau}_{y=0} = \frac{U}{1+(\frac{\theta}{20})^2}S_{2/2}(\theta) + \frac{(\frac{\theta}{20})^2}{1+(\frac{\theta}{20})^2}\frac{U}{2\sqrt{\pi}}$ where $S_{2/2}(\theta)$ is specified in Eq. (104)
$N = 2$ polynomial expansion including gain-free term	Bulk velocity Eq. (54)	$\tilde{u}_x = \frac{1}{\pi^{3/2}}\int_{c_{y,1}>0} c_{y,1}\hat{h}^{\mathrm{I}}(\mathbf{c}_1)e^{-c_1^2}d\mathbf{c}_1 + \frac{1}{\pi^{3/2}}\int_{c_{y,1}<0} c_{y,1}\hat{h}^{\mathrm{II}}(\mathbf{c}_1)e^{-c_1^2}d\mathbf{c}_1$ where $\hat{h}^{\mathrm{I}}$ and $\hat{h}^{\mathrm{II}}$ are the solution to Eq. (99)
	Shear stress Eq. (64)	$\tilde{\tau}_x = \frac{1}{\pi^{3/2}}\int_{c_{y,1}>0} c_{x,1}c_{y,1}\hat{h}^{\mathrm{I}}(\mathbf{c}_1)e^{-c_1^2}d\mathbf{c}_1 + \frac{1}{\pi^{3/2}}\int_{c_{y,1}<0} c_x c_{y,1}\hat{h}^{\mathrm{II}}(\mathbf{c}_1)e^{-c_1^2}d\mathbf{c}_1$ where $\hat{h}^{\mathrm{I}}$ and $\hat{h}^{\mathrm{II}}$ are the solution to Eq. (99)

generalizing the method to encompass complex solutions of the frequency-domain Boltzmann equation. A systematic method was outlined, allowing solutions to general problems with no prior knowledge of the flow.

This method was applied to two one-dimensional flows: first, the derivation of analytical formulas (62) and (73) for oscillatory Couette flow, and second, the derivation of simple systems of ordinary differential equations (99) and a simple shear stress formula (103) for Stokes' second problem. These results are summarized in Table III. In each case a good approximation is obtained over a wide range of Knudsen numbers and oscillation frequencies. While in this article we have focused on one-dimensional flows, an analysis of a rectilinearly oscillating sphere will be left for future work.

The principal advantage of this variational approach is its ability to generate simple formulas for unsteady rarefied flows that would otherwise require the use of advanced computational techniques. This can be advantageous in practical application.

ACKNOWLEDGMENTS

This research was supported by the Australian Research Council Centre of Excellence in Exciton Science (CE170100026) and the Australian Research Council Grants Scheme.

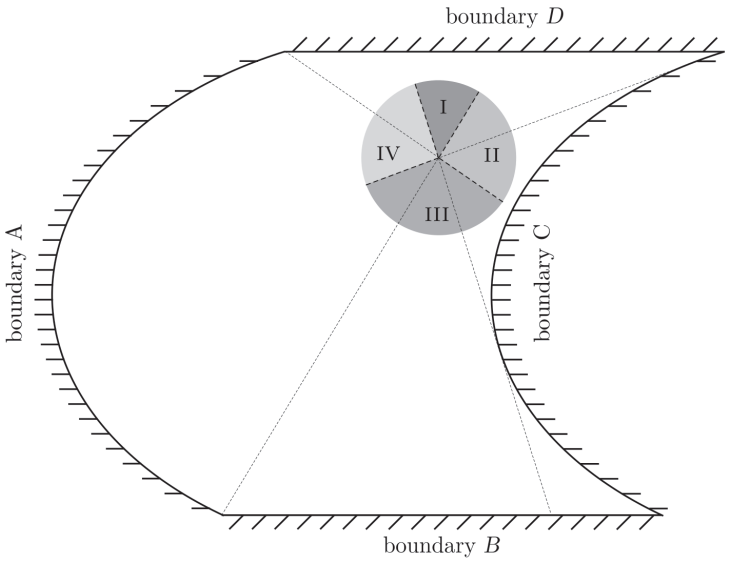

FIG. 10. Illustration of an example trial function where curved boundaries are present. For arbitrary position $\mathbf{x}$, particle velocities emanating from boundary A pass through shaded region II, particle velocities emanating from boundary B pass through region I, particle velocities emanating from boundary C pass through region IV, and particle velocities emanating from boundary D pass through region III. The heavy dashed lines represent discontinuities in particle velocity space. The light dashed lines trace the particle velocities from the locations where discontinuities are induced by the boundaries $\mathbf{x}$. Note that a discontinuity is induced by the horizon of the convex boundary C; however, no change occurs due to the concavity introduced into boundary A when compared to the straight boundary used in Fig. 1.

APPENDIX: TRIAL FUNCTION FOR ARBITRARY BOUNDARY SHAPES

In Sec. IV A we defined a trial function $\hat{h}$ that is piecewise in particle velocity space. Figure 1 illustrates how each segment of this piecewise function, i.e., $\hat{h}^{\mathrm{p}}(\mathbf{c},\mathbf{x})$, corresponds to the characteristics emanating from a given boundary. For simplicity, a spatial domain with straight boundaries was used in Sec. IV A. In this Appendix we demonstrate the applicability of the approach to boundaries of arbitrary shape.

In Fig. 10 the geometry of Fig. 1 is modified by changing boundaries A and C from straight lines to concave and convex curves, respectively. In Fig. 1 lines may be drawn directly from any spatial point inside the domain to the ends of boundary C, which extends from the top right to the bottom right corner of the domain. At the spatial point illustrated in Fig. 10, it is still possible to draw a straight line to the top end of boundary C; however, the bottom end is obscured due to the convex shape. The particle velocities emanating from boundary C, shown by shaded region IV, therefore range from the characteristic emanating from the top right corner to the characteristic which touches the horizon of boundary C. This shadowing effect will occur in the vicinity of any convex boundary.

[1] Y. Yang, C. Callegari, X. Feng, K. Ekinci, and M. Roukes, Zeptogram-scale nanomechanical mass sensing, Nano Lett. **6**, 583 (2006).

[2] I. Bargatin, I. Kozinski, and M. L. Roukes, Efficient electrothermal actuation of multiple modes of high-frequency nanoelectromechanical resonators, Appl. Phys. Lett. **90**, 093116 (2007).

[3] K. Jenses, K. Kim, and A. Zettl, An atomic-resolution nanomechanical mass sensor, Nat. Nanotechnol. **3**, 533 (2008).
[4] G. Binnig, C. F. Quate, and C. Gerber, Atomic Force Microscope, Phys. Rev. Lett. **56**, 930 (1986).
[5] F. J. Giessibl, Advances in atomic force microscopy, Rev. Mod. Phys. **75**, 949 (1986).
[6] J. E. Sader, Frequency response of cantilever beams immersed in viscous fluids with applications to the atomic force microscope, J. Appl. Phys. **84**, 64 (1998).
[7] S. Boskovic, J. W. M. Chon, P. Mulvaney, and J. E. Sader, Rheological measurements using microcantilevers, J. Rheol. **46**, 891 (2002).
[8] M. Pelton, D. Chakraborty, E. Malachosky, P. Guyot-Sionnest, and J. E. Sader, Viscoelastic Flows in Simple Liquids Generated by Vibrating Nanostructures, Phys. Rev. Lett. **111**, 244502 (2013).
[9] R. Berger, C. Gerber, H. P. Lang, and J. K. Gimzewski, Micromechanics: A toolbox for femtoscale science: 'Towards a laboratory on a tip', Microelectron. Eng. **35**, 373 (1997).
[10] N. V. Lavrik, M. J. Sepaniak, and P. G. Datskos, Cantilever transducers as a platform for chemical and biological sensors, Rev. Sci. Instrum. **75**, 2229 (2004).
[11] R. J. Dolleman, D. Davidovikj, S. J. Cartamil-Bueno, H. S. van der Zant, and P. G. Steeneken, Graphene squeeze-film pressure sensors, Nano Lett. **16**, 568 (2015).
[12] Y. Sone, *Kinetic Theory and Fluid Dynamics* (Birkhäuser, Basel, 2000).
[13] C. Cercignani and C. D. Pagani, Variational approach to boundary-value problems in kinetic theory, Phys. Fluids **9**, 1167 (1966).
[14] J. H. Ferziger, Flow of a rarefied gas through a cylindrical tube, Phys. Fluids **10**, 1448 (1967).
[15] C. Cercignani, C. Pagani, and P. Bassanini, Flow of a rarefied gas past an axisymmetric body. II. Case of a sphere, Phys. Fluids **11**, 1399 (1968).
[16] C.-L. Su, Variational principles for the heat flux in a rarefied gas between concentric cylinders, Phys. Fluids **11**, 2144 (1968).
[17] S. K. Loyalka and J. H. Ferziger, Model dependence of the slip coefficient, Phys. Fluids **10**, 1833 (1967).
[18] S. K. Loyalka and J. H. Ferziger, Model dependence of the temperature slip coefficient, Phys. Fluids **11**, 1668 (1968).
[19] I. B. Bernstein, Variational calculation of transport coefficients in a binary mixture, Phys. Fluids **12**, 64 (1969).
[20] P. Riesco-Chueca and J. F. De La Mora, Variational determination of the coefficient of sound dispersion in binary gas mixtures, J. Fluid Mech. **188**, 205 (1988).
[21] C. Cercignani, A variational principle for boundary value problems in kinetic theory, J. Stat. Phys. **1**, 297 (1969).
[22] C. Cercignani, M. Lampis, and S. Lorenzani, Variational approach to gas flows in microchannels, Phys. Fluids **16**, 3426 (2004).
[23] C. Cercignani, M. Lampis, and S. Lorenzani, in *Proceedings of the 23rd International Symposium on Rarefied Gas Dynamics*, edited by A. D. Ketsdever and E. P. Muntz, AIP Conf. Proc. No. 663 (AIP, Melville, 2003), pp. 141–148.
[24] C. Cercignani, M. Lampis, and S. Lorenzani, Plane Poiseuille-Couette problem in micro-electro-mechanical systems applications with gas-rarefaction effects, Phys. Fluids **18**, 087102 (2006).
[25] C. Cercignani and S. Lorenzani, Variational derivation of second-order slip coefficients on the basis of the Boltzmann equation for hard-sphere molecules, Phys. Fluids **22**, 062004 (2010).
[26] S. Lorenzani, Higher order slip according to the linearized Boltzmann equation with general boundary conditions, Philos. Trans. R. Soc. A **369**, 2228 (2011).
[27] D. R. Ladiges, Oscillatory rarefied flows: Monte Carlo and variational methods, Ph.D. thesis, University of Melbourne, 2016.
[28] A. Frezzotti, L. Gibelli, and B. Franzelli, A moment method for low speed microflows, Continuum Mech. Thermodyn. **21**, 495 (2009).
[29] C. Cercignani, *Mathematical Methods in Kinetic Theory* (Springer, Berlin, 1969).
[30] C. Cercignani, *The Boltzmann Equation and its Applications* (Springer, Berlin, 1988).
[31] P. L. Bhatnagar, E. P. Gross, and M. Krook, A model for collision processes in gases. I. Small amplitude processes in charged and neutral one-component systems, Phys. Rev. **94**, 511 (1954).

[32] J. C. Maxwell, On stresses in rarified gases arising from inequalities of temperature, Philos. Trans. R. Soc. London **170**, 231 (1879).
[33] C. Cercignani and M. Lampis, Kinetic models for gas-surface interactions, Transp. Theor. Stat. Phys. **1**, 101 (1971).
[34] D. R. Ladiges and J. E. Sader, Frequency-domain deviational Monte Carlo method for linear oscillatory gas flows, Phys. Fluids **27**, 102002 (2015).
[35] S. Naris and D. Valougeorgis, The driven cavity flow over the whole range of the Knudsen number, Phys. Fluids **17**, 097106 (2005).
[36] F. Sharipov and D. Kalempa, Oscillatory Couette flow at arbitrary oscillation frequency over the whole range of the Knudsen number, Microfluid. Nanofluid. **4**, 363 (2008).
[37] M. Abramowitz and I. A. Stegun, *Handbook of Mathematical Functions: With Formulas, Graphs, and Mathematical Tables* (Courier, Mineola, 1964), p. 55.
[38] Y. W. Yap and J. E. Sader, High accuracy numerical solutions of the Boltzmann Bhatnagar-Gross-Krook equation for steady and oscillatory Couette flows, Phys. Fluids **24**, 032004 (2012).
[39] Y. Shi, Y. W. Yap, and J. E. Sader, Lattice Boltzmann method for linear oscillatory non-continuum flows, Phys. Rev. E **89**, 033305 (2014).
[40] G. K. Batchelor, *An Introduction to Fluid Dynamics* (Cambridge University Press, Cambridge, 2000).
[41] Y. Sone, in *Rarefied Gas Dynamics*, edited by L. Trilling and H. Y. Wachman (Academic, New York, 1969), Vol. 1, p. 243.
[42] J. Nassios and J. E. Sader, Asymptotic analysis of the Boltzmann–BGK equation for oscillatory flows, J. Fluid Mech. **708**, 197 (2012).
[43] N. G. Hadjiconstantinou, G. A. Radtke, and L. L. Baker, On variance reduced simulations of the Boltzmann transport equation for small-scale heat transfer applications, J. Heat Transfer **132**, 112401 (2010).
[44] G. A. Radtke and N. G. Hadjiconstantinou, Variance-reduced particle simulation of the Boltzmann transport equation in the relaxation-time approximation, Phys. Rev. E **79**, 056711 (2009).
[45] See Supplemental Material at http://link.aps.org/supplemental/10.1103/PhysRevFluids.3.053401 for the complete solution, available in a *Mathematica* file.
[46] F. Sharipov and D. Kalempa, Gas flow near a plate oscillating longitudinally with an arbitrary frequency, Phys. Fluids **19**, 017110 (2007).
[47] F. Sharipov and V. Seleznev, Data on internal rarefied gas flows, J. Phys. Chem. Ref. Data **27**, 657 (1998).
[48] D. R. Ladiges and J. E. Sader, Frequency-domain Monte Carlo method for linear oscillatory gas flows, J. Comput. Phys. **284**, 351 (2015).